




Article

Multilevel Algorithm for Large-Scale Gravity Inversion

Shujin Cao ^{1,2,3,†} , Peng Chen ^{1,†}, Guangyin Lu ^{2,*} , Yajing Mao ¹ , Dongxin Zhang ², Yihuai Deng ¹ and Xinyue Chen ¹

¹ School of Earth Sciences and Spatial Information Engineering, Hunan University of Science and Technology, Taoyuan Road, Xiangtan 411201, China; shujin.cao@hnust.edu.cn (S.C.); pengchen@mail.hnust.edu.cn (P.C.); mao-yajing@mail.hnust.edu.cn (Y.M.); yihuai.deng@mail.hnust.edu.cn (Y.D.); chenxinyue@hnust.edu.cn (X.C.)

² School of Geosciences and Info-Physics, Central South University, Lushan South Road, Changsha 410083, China; zdx_csu@163.com

³ Institute of Geophysics & Geomatics, China University of Geosciences, Wuhan 430074, China

* Correspondence: luguangyin@csu.edu.cn

† These authors contributed equally to this work.

Abstract: Surface gravity inversion attempts to recover the density contrast distribution in the 3D Earth model for geological interpretation. Since airborne gravity is characterized by large data volumes, large-scale 3D inversion exceeds the capacity of desktop computing resources, making it difficult to achieve the appropriate depth/lateral resolution for geological interpretation. In addition, gravity data are finite and noisy, and their inversion is ill posed. Especially in the absence of a priori geological information, regularization must be introduced to overcome the difficulty of the non-uniqueness of the solutions to recover the most geologically plausible ones. Because the use of Haar wavelet operators has an edge-preserving property and can preserve the sensitivity matrix structure at each level of the multilevel method to obtain faster solvers, we present a multilevel algorithm for large-scale gravity inversion solved by the re-weighted regularized conjugate gradient (RRCG) algorithm to reduce the inversion computational resources and improve the depth/lateral resolution of the inversion results. The RRCG-based multilevel inversion was then applied to synthetic cases and airborne gravity data from the Quest-South project in British Columbia, Canada. Results from synthetic models and field data show that the RRCG-based multilevel inversion is suitable for obtaining density contrast distributions with appropriate horizontal and vertical resolution, especially for large-scale gravity inversions compared to Occam's inversion.

Keywords: extension equivalent geometric framework; rapid forward; multilevel; large-scale inversion; Haar wavelets



Citation: Cao, S.; Chen, P.; Lu, G.; Mao, Y.; Zhang, D.; Deng, Y.; Chen, X. Multilevel Algorithm for Large-Scale Gravity Inversion. *Symmetry* **2024**, *16*, 758. <https://doi.org/10.3390/sym16060758>

Academic Editors: Marcio Basilio and Valdecy Pereira

Received: 10 April 2024

Revised: 2 June 2024

Accepted: 14 June 2024

Published: 17 June 2024



Copyright: © 2023 by the authors. Licensee MDPI, Basel, Switzerland. This article is an open access article distributed under the terms and conditions of the Creative Commons Attribution (CC BY) license (<https://creativecommons.org/licenses/by/4.0/>).

1. Introduction

Airborne gravity surveys are characterized by very large data volumes, typically containing hundreds to thousands of kilometers of data lines with points every few meters, covering areas of thousands of square kilometers [1]. However, due to the limited computing resources of desktop equipment and the high computational cost of forward and inverse algorithms, large-scale gravity field inversions cannot achieve the appropriate resolution and level of detail required for geological interpretation [2,3]. There are two main ways to acquire forward operators (Jacobi, kernel, or sensitivity matrix) for gravitational fields. Firstly, the forward operator can be constructed directly from the discretized integral equations/integral equations, which are Poisson's integral approach [4], Green's integral approach [5], radial multipole approach [6], point-mass approach [7], and single-layer approach [8]. The 2D/3D Earth model is discretized into simple geometries such as triangles [9], rectangles [10], tetrahedrons [11], point masses [12], right rectangular prisms, or right polygonal prisms [13], which have analytical solutions that are used to compute self-induced gravity effects and gravity gradients. Contributions from anomaly

sources are obtained using the discretized integral equations/integral equations based on the principle of superposition [14–16]. Secondly, the forward operator of gravitational fields can be recovered indirectly based on partial differential equations (PDEs), such as the finite-difference method [17,18], the finite-element method [19], and the finite-volume method [20]. The gravitational field is acquired using PDEs; then, the gravitational anomalies and higher-order derivatives of the gravitational field are calculated using first-order and high-order difference operations. However, the right-hand-side term of Poisson's equation becomes more complicated during the inverse iteration as the number of prismatic cells with non-zero density increases, and its computation time increases sharply with the number of prismatic cells or observation points. Therefore, the forward modeling algorithm via discretized integral equations/integral equations is often used for the inversion of gravity/tensor gravity data. The computational cost of optimizing the objective function established by the physical property inversion is considerable in the face of requirements such as 3D fine geotectonic studies at large scales, multiple areas, and large volumes of data [1,21–23].

To meet the needs of large-scale fast 3D inversion, the current fast inversion research is mainly carried out by dimensionality reduction and improving the computational performance of the equipment. First, dimensionality reduction methods are used to reduce the memory consumption of the kernel matrix and improve the computational efficiency, i.e., using techniques such as equivalent geometric framework [24], wavelet transforms [3], footprint inversion [1] and fast Fourier transform (FFT) [25], and planting inversion to change the implementation of the kernel matrix, which can significantly improve the efficiency of the inversion implementation while reducing the required memory space of the kernel matrix. However, all these methods have some limitations, such as the fact that the equivalent geometric framework depends on the symmetry of the potential field, the wavelet algorithm may reduce the computational accuracy, and the planting inversion is overly dependent on the inversion parameter settings. Second, large-scale parallel acceleration research is being carried out on multi-core CPU, cluster computer, and GPU platforms to improve the ability of computing devices to process massive matrix operations, thereby effectively reducing inversion computation time [2,26,27]. However, its hardware and software access threshold is relatively high, and only a few research results have been published. Third, the constraint function speeds up the convergence of the inversion iteration. For example, the reconstruction density contrast distribution is optimized by the depth-weighting function [28] and the fast convergence of the objective function is ensured by applying the preprocessing matrix [29].

Similar to other geophysical inversion methods, the current gravity and magnetic inversion methods and their gradient/tensor inversion methods mainly face the problem of the non-uniqueness of the solution. To make the ill-conditioned problem converge to a well-conditioned system, the constraint function is generally constructed by imposing regularization terms on the objective function, such as L0- [30], L1- [31], L2- [28,32], and LP- [33] norm minimization, to impose a priori geological information to obtain a density contrast distribution close to the actual situation. However, due to the lack of a priori geological information, the inversion results mainly depend on the choice of the constraint function. For example, affected by the smoothing effect, the traditional property inversion method based on a minimization of sum-of-squares, or L2-norm, is smooth in both the vertical and horizontal directions [34]. In order to accurately highlight the geological structure and meet the needs of 3D delicate structure inversion, various methods have been developed and have achieved certain results, such as total variation regularization inversion [35,36], focusing inversion [37], sharp boundary inversion [38], and steep boundary inversion [39]. Tikhonov regularization based on the L2 norm has the advantages of fast imaging speed and a stable solution; however, there are existing problems, e.g., the imaging effect is not good, poor resolution, and difficulty distinguishing between adjacent abnormal sources [28]. Total variation regularization based on the L1 norm can make the boundary between the target area and the background area of the reconstructed

image clearer [40]. However, there are some shortcomings, such as insufficient convergence of the objective function and inaccurate positioning of the target area [41]. Sharp boundary inversion [38,42] has shortcomings, e.g., inaccurate inversion of deep structure and difficulty adding constraints. However, it can achieve excellent inversion results when the geological prior information is sufficient. These methods all have a certain emphasis, i.e., they have a single advantage for the corresponding problems. Then, in the face of more complex geological structures, this advantage will become a deficiency. In addition to the problems described above, focusing inversion can generally obtain better depth resolution.

Regardless of the inversion technique used, all geological constraints manifest themselves as a regularization that can be quantified by an a priori model, data weights, model weights, upper and lower bounds [43–46], and the type of stabilizing function [47–49]. The stabilizing function should be chosen by the user, taking into account geological knowledge, as well as information about the class of models from which a unique solution is sought [1,50]. In order to reconstruct a feasible geological image of the subsurface, it is common practice to place lower and upper bounds on the variables while managing the ambiguity of the geophysical potential field inversion problem [37,51,52]. A priori information on the density distribution serving as the inversion bounds is critical when using focusing inversion [12,53]. Different results are obtained when different upper and lower density bounds are used [54]. Numerical tests show that focusing inversion produces a stable solution, but tends to produce the smallest possible anomalous domain. It also makes the image look unrealistically sharp [37], i.e., overfocused. Therefore, in order to avoid the overfocused phenomenon, in the focusing inversion algorithm verification, the upper density bound is usually the maximum value of the model parameters, and the lower density bound is the background value of the model [37]. In practical applications, geological data or human judgment has often been used to determine the upper and lower density bounds [50,55]. Essentially, each method has a different physical basis. That is, it has a single significant advantage for the corresponding problem, and, in the face of more complex geological structures, this advantage turns into an over-regularization effect [37].

Therefore, in the present work, to avoid over-regularization effects, we introduce the wavelet transform into the large-scale potential field inversion to extract geotectonic boundaries. In general, the wavelet transform can only reflect the singularity and non-singularity of zero-dimensional data, making it difficult to characterize high-dimensional data [56–58]. Therefore, the characteristics of discontinuous strata may be blurred in 3D inversion after wavelet transform filtering (a transform-based method) [59]. To overcome this difficulty of wavelet transforms, some multi-scale analysis methods have been developed in recent years, such as ridgelets, curvelets, and so on. Li and Hu [60] improved the image denoising method for synthetic aperture radar images using the curvelet wavelet transform for the inherent defects, which make it difficult for the wavelet transform to express the directional characteristics of image edges, which significantly improves the effect and processing speed of noise suppression. Compared with wavelet analysis, the 3D discrete curvelet transform has directional characteristics, which can better describe the singularity of the edge surface and has better sparse performance [61]. To obtain a clear and undistorted geological interface, Liu et al. [62] subtracted the extracted background field from the magnetotelluric observation data to obtain a residual field containing local details. The thresholding technique eliminates high-frequency noise from the wavelet decomposition resulting from the residual field to preserve its higher energy components to generate the local details. The focusing inversion characterizes the local details, and the inversion smooths the background field to reduce the computational time of the inversion. Like geophysical inversion, image multi-scale target detection methods based on a multi-scale pyramid divide the original image/data into multiple scales. It can detect the target without prior knowledge. Then, through integration/fusion of the detection results of each scale, the detection accuracy is improved [63]. However, for massive data, similar to algebraic multigrid, the traditional pyramid method is time-consuming and inefficient [64].

It is widely acknowledged that the multilevel method represents the optimal approach for addressing a range of geophysical challenges [65,66]. Currently, the multilevel method is one of the most important methods to deal with ill-posed problems in the field of geophysics [67–71]. However, the classical multilevel method can no longer be applied to solve ill-posed problems. Consequently, researchers have initiated efforts to identify novel avenues for advancement. The characteristics of multilevel methods have enabled the achievement of some breakthroughs and research results in image denoising, signal reconstruction, and edge preservation. For example, based on the multigrid method, Buccini and Donatelli [67] propose a denoising method combining L2-regularization and an iterative soft threshold algorithm that uses a fast Fourier transform for frequency filtering, and the reconstruction of sparse signals is completed in the wavelet domain. In this process, the multigrid method is used to ensure the stability of convergence and denoising. The advantage of this method is that it can be employed as a post-smooth soft thresholding for denoising, i.e., it can provide high-precision signal reconstruction for a variety of different scenarios without setting any parameters. Chu et al. [70] proposed new extrapolation economy cascadic multigrid method, which provides a more accurate initial value for the fine grid layer by combining the new extrapolation formula with the quadratic interpolation and is applied to solve the image restoration model. This method not only removes the noise while maintaining the image edge but also reduces the number of iterations and the staircase effect while ensuring accuracy, which can improve computational efficiency and have better recovery quality.

The structure of the paper is as follows. In Section 2, we first briefly describe the principles of the forward and inversion problems, and Occam's inversion for gravity/tensor gravity data. In Section 3, we propose a new extension technique that exploits the translational equivalence of gravitational fields to avoid relying on the symmetry of potential fields, to efficiently perform the forward modeling of gravity/tensor gravity data. In Section 4, concerning the work of Español and Kilmer [68], we outline a generic multilevel algorithm for large-scale gravity inversion, propose an efficient construction method for restriction operators, and address some of the inversion issues of recovering depth resolutions. Sections 5 and 6 analyze the computational performance of the rapid forward method. In Section 7, we constructed a set of synthetic models to verify the correctness of the RRCCG algorithm used in this paper. Sections 8–11 contain numerical results. In Section 12, we conducted a model plausibility analysis, i.e., utilize histograms to assess the reasonableness of the recovered models, and Section 13 summarizes conclusions and suggestions.

2. Principles of Regularized Inversion of Gravity/Tensor Gravity Data

In Figure 1, there are two 3D Cartesian coordinate systems: the ξ and x axes point northward; the η and y axes point eastward; and the ζ and z axes point positively downward. In the 3D property inversion, the 3D interpretation model is discretized into prismatic cells (blue wireframe) with homogeneous density, whose side lengths are Δx , Δy , and Δz , respectively. Their sections along the three axes are n_x , n_y , and n_z , respectively. The coordinates of the centroid of a prismatic cell Q (see Figure 2) are denoted as (ξ, η, ζ) , and its corresponding index is $\langle l, m, n \rangle$. The coordinates of the observation point P are denoted as (x, y, z) , and its corresponding index is $\langle p, q, t \rangle$.

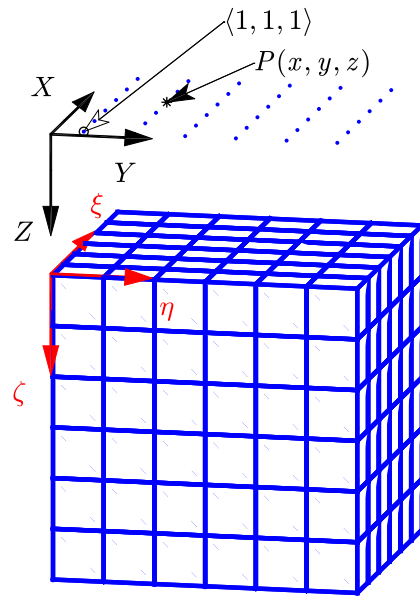


Figure 1. A 3D interpretation model is discretized into prismatic cells (blue wireframe) with constant density.

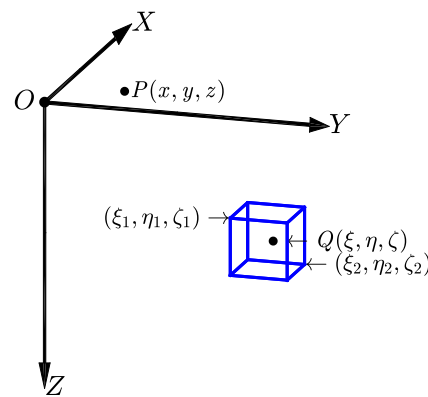


Figure 2. Gravitational attraction at observation point P is due to a prismatic cell Q with a constant density.

Using discrete model parameters and discrete data, the forward modeling operator for the gravity field can be expressed in matrix form:

$$d = Gm \tag{1}$$

where d is a vector of the observed data vector, such as $g_x, g_y, g_z, g_{xx}, g_{xy}, g_{xz}, g_{yx}, g_{yy},$ or g_{yz} , and its order is N_d ; m is an N_m order vector of model parameters (i.e., densities ρ); the size of the sensitivity matrix G is $N_d \times N_m$. Here, the number of prismatic cells is $N_m = n_x \times n_y \times n_z$ and the number of observation points $N_d = n_x \times n_y$.

According to potential theory, the gravitational contribution of all prismatic cells with densities at the i -th observation point is given by

$$d_i = \sum_{j=1}^{N_m} G_{ij} \rho_j \tag{2}$$

where the kernel function G_{ij} corresponds to the gravitational effect induced by the j -th prismatic cell with density ρ_j at the i -th observation point. $i = p + (q - 1)n_x + (t - 1)n_x n_y$, $1 \leq p \leq n_x, 1 \leq q \leq n_y, 1 \leq t \leq n_z$; $j = l + (m - 1)n_x + (n - 1)n_x n_y$, $1 \leq l \leq n_x$, and $1 \leq m \leq n_y, 1 \leq n \leq n_z$.

The inverse problem of gravity/tensor gravity data is ill posed, i.e., the solution may be non-unique and unstable. Therefore, the methods of regularization theory are usually used to solve this problem. For simplicity, the solution of the linear inverse problem (1) is replaced by the minimization of the Tikhonov parametric function

$$P^\alpha(m) = \phi_d(m) + \alpha\phi_m(m) = \min \quad (3)$$

where the regularization parameter α ($\alpha > 0$) is essential and is determined using the generalized cross-validation with the random trace estimation method [3], $\phi_d(m) = \|W_d(Gm - d)\|^2$ represents a data misfit (a data misfit is defined by a least-squares measure) functional, which is determined as the square norm of the observed and predicted data discrepancies; the model misfit function $\phi_m(m)$ is also known as the model roughness, and W_d is the data weighting matrix.

Due to their algorithmic stability and smooth results, Occam's-style algorithms are used to solve Equation (3). Occam's inversion is a practical algorithm that utilizes model roughness to construct an objective function $P^\alpha(m)$ to generalize smooth models from geophysical data [32]. The problem of minimizing the objective function is solved by making the derivative of $P^\alpha(m)$ concerning Δm equal to 0, which yields

$$\left[W_d^T G^T G W_d + \alpha (W_z^T R_m^T R_m W_z) \right] \Delta m = G^T \Delta d \quad (4)$$

where $\Delta m = m - m_{ref}$, $\Delta d = d - Gm_{ref}$, m_{ref} is the reference model, and $R_m^T R_m = \alpha_s R_s^T R_s + \alpha_x R_x^T R_x + \alpha_y R_y^T R_y + \alpha_z R_z^T R_z$. Here, T is the matrix transposition operation and flatness α_s , α_x , α_y , and α_z are coefficients that affect the relative importance of different terms in the objective function. The diagonal matrix R_s is the identity matrix for the reference model m_{ref} , and the sparse matrices R_x , R_y , and R_z are the difference operators along the x -, y -, and z -axes, respectively. The depth matrix $diag(W_z) = (z + z_0)^{-\beta/2}$ counteracts the natural decay of the sensitivity matrix, so that the inversion yields depth information. Here, z is the centroid depth of the prismatic cells, and the decay index β depends on the potential field. The prismatic cell size and the observation height determine the scalar z_0 . The main diagonal W_d contains the total absolute error:

$$W_d = diag(|d| \cdot SD(d) + \varepsilon)^{-1} \quad (5)$$

where $diag()$ represents the input of a vector, which will result in a diagonal matrix (i.e., sparse matrix) with this vector as the main diagonal element; $SD(d)$ is the standard deviation of the observed data, and ε is a tiny constant that prevents the inversion from placing too much weight on very low amplitude data. Equation (4) is a large system of linear equations for geophysical inversion. To obtain m , this system must be solved iteratively until the convergence condition is satisfied. Thus, the number of kernel functions for the sensitivity matrix G that needs to be stored is given by

$$N_G^1 = N_d \times N_m = (n_x \times n_y) \times (n_x \times n_y \times n_z) \quad (6)$$

Since surface gravity data contain no or little depth resolution information [28], and Occam's-style algorithms, such as smooth inversion, marquardt inversion, and Occam's inversion [28,72], which have difficulty recovering depth resolution information even if the depth-weighting function is used. To overcome this difficulty, the multilevel inversion, in conjunction with the re-weighted regularized conjugate gradient (RRCG), is proposed in Section 4 to recover the resolution of the interpretation model in both vertical and horizontal directions.

3. Forward Calculation Technology of Gravity/Tensor Gravity Data

3.1. Analytical Solution of Gravity/Tensor Gravity Data

For completeness, we briefly introduce gravity and full tensor gravity (FTG) for constructing the forward modeling operators (see Equation (1)). The gravity field g satisfies equations in gravity surveys [73]:

$$\nabla \cdot g = -4\pi v\rho, \nabla \times g = 0 \quad (7)$$

where $v = 6.672 \times 10^{-11} \text{ N}\cdot\text{m}^2/\text{kg}^2$ is gravitational constant. According to $\nabla \times g = 0$ in a region, g is an irrotational field, that is, a vector field is irrotational over the region if its curl vanishes at every point in the region.

The gravity vector (g_x , g_y , and g_z) is the spatial rate of change in gravitational acceleration. The FTG is the spatial rate of change of gravity vectors, which can also be measured by a gravity gradiometer and is denoted as

$$\Gamma = \begin{bmatrix} g_{xx} & g_{xy} & g_{xz} \\ g_{yx} & g_{yy} & g_{yz} \\ g_{zx} & g_{zy} & g_{zz} \end{bmatrix} \quad (8)$$

Since, in source-free space [74], the potential field is irrotational [75], that is, $\nabla \times (\nabla \cdot g) = 0$ (see Equation (7)), and the potential's tensor is symmetric and traceless due to Laplace's equation, that is, $g_{xx} + g_{yy} + g_{zz} = 0$, $g_{xy} = g_{yx}$, $g_{xz} = g_{zx}$, and $g_{yz} = g_{zy}$. Therefore, Γ has only five independent components, i.e., g_{xx} , g_{xy} , g_{xz} , g_{yy} , and g_{yz} , as shown in Equation (8).

Taking the calculation of the forward modeling of gravity anomalies as an example, as shown in Figures 1 and 2, the analytical solution for gravity anomalies at an observation point P due to a prismatic cell Q with density $\rho_{(\xi,\eta,\zeta)}$ is [13]

$$g_z = -v\rho_{(\xi,\eta,\zeta)} \sum_{\bar{i}=1}^2 \sum_{\bar{j}=1}^2 \sum_{\bar{k}=1}^2 \mu_{\bar{i}\bar{j}\bar{k}} \times \left[x_{\bar{i}} \ln(y_{\bar{j}} + r_{\bar{i}\bar{j}\bar{k}}) + y_{\bar{j}} \ln(x_{\bar{i}} + r_{\bar{i}\bar{j}\bar{k}}) + z_{\bar{k}} \tan^{-1} \left(\frac{z_{\bar{k}} r_{\bar{i}\bar{j}\bar{k}}}{x_{\bar{i}} y_{\bar{j}}} \right) \right] \quad (9)$$

where $\mu_{\bar{i}\bar{j}\bar{k}} = (-1)^{\bar{i}+\bar{j}+\bar{k}}$, $x_{\bar{i}} = x - \xi_{\bar{i}}$, $y_{\bar{j}} = y - \eta_{\bar{j}}$, $z_{\bar{k}} = z - \zeta_{\bar{k}}$, and $r_{\bar{i}\bar{j}\bar{k}} = \sqrt{x_{\bar{i}}^2 + y_{\bar{j}}^2 + z_{\bar{k}}^2}$.

3.2. Rapid Forward Modeling of Gravity/Tensor Gravity Data

3.2.1. Equivalent Geometric Framework

Figure 3 shows two surveys available for the 3D inversion of potential field data. A traditional survey employs single-layer observation points (e.g., black dots in Figure 1, and those dots form blue surfaces in Figure 3a) across all prismatic cells of a 3D interpretation model. Additionally, the equidimensional inversion is created by multi-layer observation points across all prismatic cells of the 3D interpretation model [76]. The inversion synthesizes the potential field data at different heights in order to improve the depth resolution of the inversion results. Taking the first survey scheme in Figure 3a as an example, according to Equation (6), $N_G = N_d \times N_m = (1024 \times 1024) \times (1024 \times 1024 \times 1) \approx 1.1 \times 10^{12}$. It is impossible to store the kernel matrix on an existing PC, regardless of whether it is stored in double or single precision. To overcome this problem, Yao et al. [24] found that kernel functions have translation, symmetry, and interchange equivalence. Then, Equation (9) is decomposed into the density $\rho_{(\xi,\eta,\zeta)}$ and the geometric structure $K_{(\xi,\eta,\zeta)}^{(x,y,z)}$, which is a kernel function due to a prismatic cell Q at an observation point P . The geometric structure $K_{(\xi,\eta,\zeta)}^{(x,y,z)}$ of g_z can be expressed as

$$K_{(\xi,\eta,\zeta)}^{(x,y,z)} = -v \sum_{\bar{i}=1}^2 \sum_{\bar{j}=1}^2 \sum_{\bar{k}=1}^2 \mu_{\bar{i}\bar{j}\bar{k}} \times \left[x_{\bar{i}} \ln(y_{\bar{j}} + r_{\bar{i}\bar{j}\bar{k}}) + y_{\bar{j}} \ln(x_{\bar{i}} + r_{\bar{i}\bar{j}\bar{k}}) + z_{\bar{k}} \tan^{-1} \left(\frac{z_{\bar{k}} r_{\bar{i}\bar{j}\bar{k}}}{x_{\bar{i}} y_{\bar{j}}} \right) \right] \quad (10)$$

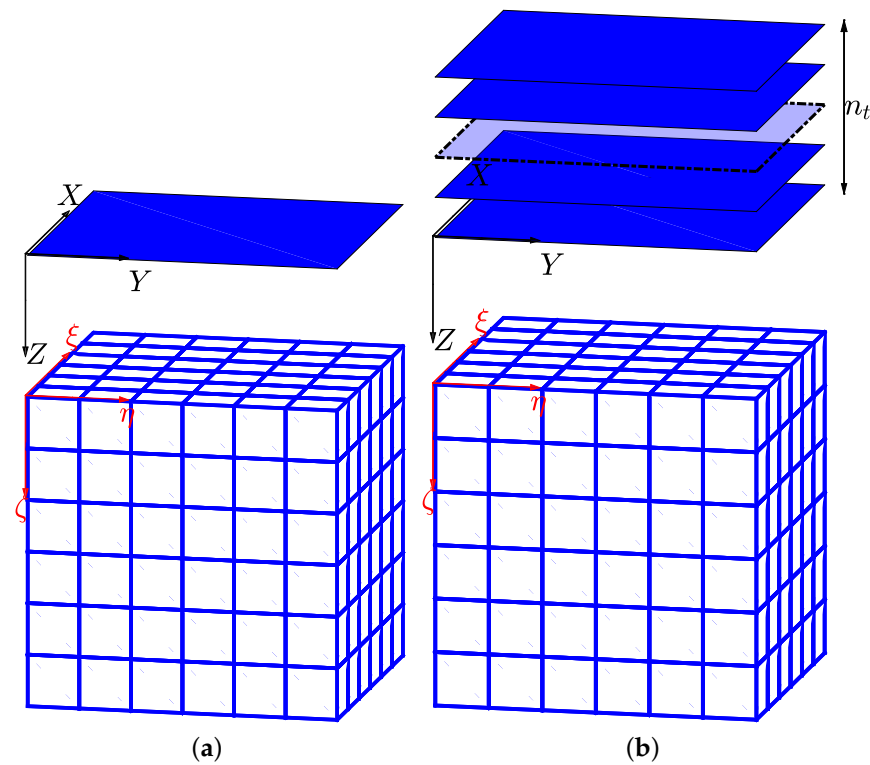


Figure 3. Two surveys. (a) Generalized inversion; (b) equidimensional inversion [76].

According to Equations (2) and (10), $K_{(\xi,\eta,\zeta)}^{(x,y,z)}$ is rewritten as $K_{\langle l,m,n \rangle}^{\langle p,q,t \rangle}$ with the corresponding indices $\langle p,q,t \rangle$ and $\langle l,m,n \rangle$ to describe more clearly the relationship between the i -th observation point P and the j -th prismatic cell Q . The kernel function has the following identity:

$$K^{i,j} \equiv K_{\langle l,m,n \rangle}^{\langle p,q,t \rangle} \equiv K_{(\xi,\eta,\zeta)}^{(x,y,z)} \tag{11}$$

where $x = (p - 1/2)\Delta x$, $y = (q - 1/2)\Delta y$, $z = -t\Delta z + H$, H is the height of the last observation surface in Figure 3b, $\xi = (l - 1/2)\Delta x$, $\eta = (m - 1/2)\Delta y$, and $\zeta = (n - 1/2)\Delta z$.

The interchange equivalence of $K_{(\xi,\eta,\zeta)}^{(x,y,z)}$ means that when the spatial positions of the observation point P and the prismatic centroid of Q are exchanged, these two kernel functions remain unchanged. This property can be expressed as follows [24]:

$$K_{(\xi,\eta,\zeta)}^{(x,y,z)} = K_{(x,y,z)}^{(\xi,\eta,\zeta)} \tag{12}$$

or

$$K_{\langle l,m,n \rangle}^{\langle p,q,t \rangle} = K_{\langle p,q,t \rangle}^{\langle l,m,n \rangle} \tag{13}$$

Symmetric equivalence means that, if two observation points (x, y, z) and (x', y', z') are symmetric about the plane passing through the center of the prismatic cell (ξ, η, ζ) and parallel to the X -axis, then these two kernel functions are equal, which can be written as [24]

$$K_{(\xi,\eta,\zeta)}^{(x,y,z)} \equiv K_{(\xi,\eta,\zeta)}^{(x',y',z')} = K_{(\xi,\eta,\zeta)}^{(2\xi-x,y,z)} \tag{14}$$

or

$$K_{\langle l,m,n \rangle}^{\langle p,q,t \rangle} \equiv K_{\langle l,m,n \rangle}^{\langle p',q',t' \rangle} = K_{\langle l,m,n \rangle}^{\langle 2l-p,q,t \rangle} \tag{15}$$

Similarly, if two observation points (x, y, z) and (x', y', z') are symmetrical about the plane passing through the center of the prismatic cell (ξ, η, ζ) and parallel to the Y -axis, they will yield

$$K_{(\xi,\eta,\zeta)}^{(x,y,z)} \equiv K_{(\xi,\eta,\zeta)}^{(x',y',z')} = K_{(\xi,\eta,\zeta)}^{(x,2\eta-y,z)} \tag{16}$$

or

$$K_{\langle l,m,n \rangle}^{\langle p,q,t \rangle} \equiv K_{\langle l,m,n \rangle}^{\langle p',q',t' \rangle} = K_{\langle l,m,n \rangle}^{\langle p,2m-q,t \rangle} \tag{17}$$

where the corresponding indices of (x', y', z') are $\langle p', q', t' \rangle$.

Translational equivalence means that, if the relative spatial positions of the observation point P and prismatic cell Q do not change, these two kernel functions remain unchanged, no matter where observation point P or prismatic cell Q is moved to [24]:

$$\begin{cases} K_{\langle l,m,n \rangle}^{\langle p,q,t \rangle} = K_{\langle l+1,m,n \rangle}^{\langle p+1,q,t \rangle} = \dots = K_{\langle l+\Delta p,m,n \rangle}^{\langle p+\Delta p,q,t \rangle} \\ K_{\langle l,m,n \rangle}^{\langle p,q,t \rangle} = K_{\langle l,m+1,n \rangle}^{\langle p,q+1,t \rangle} = \dots = K_{\langle l,m+\Delta q,n \rangle}^{\langle p,q+\Delta q,t \rangle} \\ K_{\langle l+\Delta p,m+1,n \rangle}^{\langle p+\Delta p,q+1,t \rangle} = K_{\langle l+\Delta p,m+2,n \rangle}^{\langle p+\Delta p,q+2,t \rangle} = \dots = K_{\langle l+\Delta p,m+\Delta q,n \rangle}^{\langle p+\Delta p,q+\Delta q,t \rangle} \\ \dots \end{cases} \tag{18}$$

where $1 \leq \Delta p + p \leq n_x$, $1 \leq \Delta p + l \leq n_x$, $1 \leq \Delta q + q \leq n_y$, and $1 \leq \Delta q + m \leq n_y$.

To describe the equivalent geometric framework in more detail, we consider the conventional survey (see Figure 3a), consisting of a single layer of observation points $\langle 1, 1, 1 \rangle$ and a 3D interpretation model S , as an example. We suppose that an arbitrary observation point P is moved along the green path to the observation origin point $\langle 1, 1, 1 \rangle$, as shown in Figure 4. Meanwhile, a complementary interpretation model S' (green dashed line) is created by shifting S to the observation origin point and consists of S_1, S_2, S_4 , and S_3 blocks, which are obtained by subtending the model S' by $\langle 1, 1, 1 \rangle$. The kernel functions at P , due to cells (S_2) in the first quadrant of S' , can be obtained directly. For other cells (S_1, S_3 , and S_4) located in other quadrants, the kernel functions at P cannot be obtained directly. However, by applying absolute value operations, i.e., mathematically exploiting the symmetry of the potential field, these kernel functions are obtained. Following Yao et al. [24], the equivalent geometric framework can be rewritten as follows:

$$K_{\langle l,m,n \rangle}^{\langle p,q,t \rangle} = K_{\langle |l-p|+1, |m-q|+1, n-t+1 \rangle}^{\langle 1,1,1 \rangle} \tag{19}$$

The gravitational contribution at the observation point P due to the 3D interpretation model S is equal to the gravitational contribution at $\langle 1, 1, 1 \rangle$ induced by the new 3D interpretation model. Since Equation (19) takes advantage of the absolute value operation, the three newly introduced blocks, S'_1, S'_3 , and S'_4 , are obtained by symmetrizing the blocks S_1, S_3 , and S_4 about the X-axis, the Y-axis, and the origin, respectively. In order to avoid overlapping curves and to better describe the relationship between these blocks, only S'_1 is drawn, and the outlines of the blocks, S_1, S_2, S_3, S_4 , and S'_1 are slightly offset from their centroid, as shown in Figure 4 in vertical view.

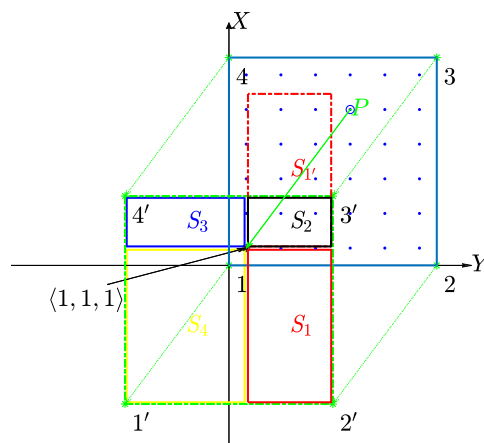


Figure 4. Diagrammatic sketch of equivalent geometric framework in vertical view.

Under the equivalent geometric framework, all observation points can be shifted to the origin point $\langle 1, 1, 1 \rangle$, according to Equation (19). The sensitivity matrix of gravitational fields can then be calculated by accumulating the kernel function values at the observation origin point $\langle 1, 1, 1 \rangle$ concerning all prismatic cells. Therefore, based on the equivalent geometric framework, the number of kernel functions that have to be stored for the sensitivity matrix is

$$N_G^2 = N_m \times N_d = (n_x \times n_y \times n_z) \times 1 \tag{20}$$

3.2.2. Extension Translational Equivalence Technique

However, since Equation (19) takes advantage of the absolute value operation, the sensitivity matrix relies on the symmetry property of gravitational fields. As shown in Figure 5, to avoid relying on the symmetry of the gravitational field, the improved 3D interpretation model V consists of the original interpretation model and three new interpretation models (with easily visible dotted lines), formed by symmetry S about the original point and the X- and Y-axes, respectively.

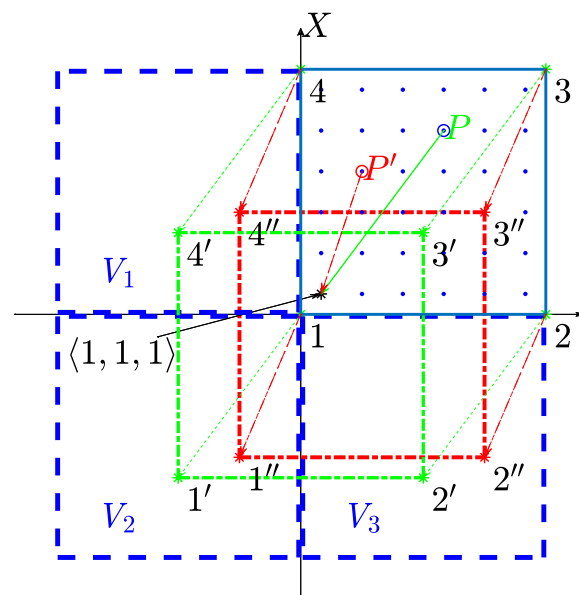


Figure 5. Diagrammatic sketch of extension translational equivalent geometric framework in vertical view.

As shown in Figure 5, a new interpretation model S' (red line) can be constructed by shifting S along the red paths. The gravitational contribution at P due to each prismatic cell of the S is then calculated by adding the gravitational effects at $\langle 1, 1, 1 \rangle$ for each prismatic cell of the S' . Therefore, it is based on translational equivalence only and is called the extension translational equivalence technique. Based on Equation (19), the kernel function obtained by using the extension translational equivalence technique can be expressed as

$$K_{\langle l,m,n \rangle}^{\langle p,q,t \rangle} = K_{\langle \tilde{l}, \tilde{m}, n-t+1 \rangle}^{\langle 1,1,1 \rangle} \tag{21}$$

where $\tilde{l} = l - p + 1$, $\tilde{m} = m - q + 1$, $-n_x + 1 \leq \tilde{l} \leq n_x$, and $-n_y + 1 \leq \tilde{m} \leq n_y$.

According to Equations (1) and (21), the number of kernel functions to be stored for the sensitivity matrix of gravitational fields based on the extension translational equivalence technique is

$$N_G^3 = N_m \times N_d = ((2n_x - 1) \times (2n_y - 1) \times n_z) \times 1 \tag{22}$$

3.2.3. Rapid Algorithm Implementation by the Extension Translational Equivalence Technique

According to Equations (2) and (11), Equation (1) can be expressed in matrix form:

$$\begin{pmatrix} K^{1,1} & \dots & K^{1,j} & \dots & K^{1,N_m} \\ \vdots & \ddots & \vdots & \ddots & \vdots \\ K^{i,1} & \dots & K^{i,j} & \dots & K^{i,N_m} \\ \vdots & \ddots & \vdots & \ddots & \vdots \\ K^{N_d,1} & \dots & K^{N_d,j} & \dots & K^{N_d,N_m} \end{pmatrix} \begin{pmatrix} \rho_1 \\ \vdots \\ \rho_j \\ \vdots \\ \rho_{N_m} \end{pmatrix} = \begin{pmatrix} d_1 \\ \vdots \\ d_i \\ \vdots \\ d_{N_d} \end{pmatrix} \quad (23)$$

As shown in Figure 6, the black line represents all observation points on the q -th survey line, and the red line represents all prismatic cells in the m -th column of the first layer of the 3D interpretation model. These two lines are parallel to the X -axis.

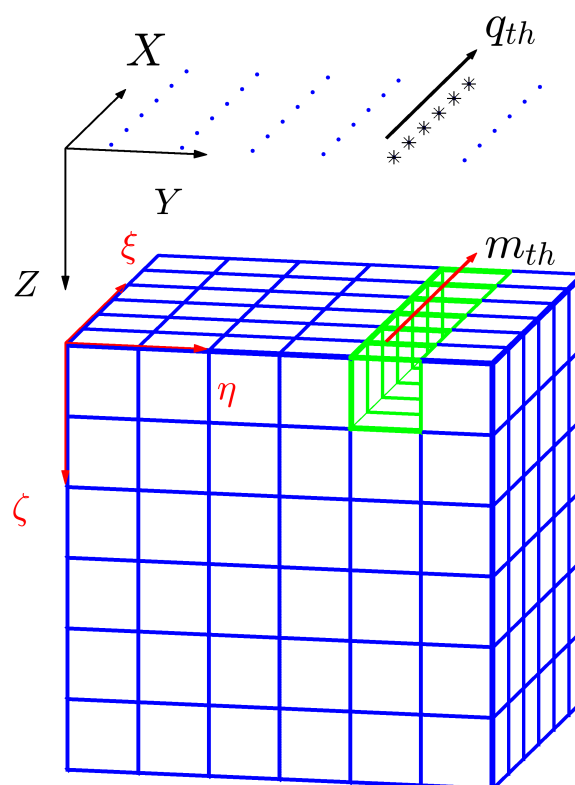


Figure 6. The Line–Line survey scheme and the Layer–Layer survey scheme.

As a Line–Line survey scheme, take the q -th survey line (black star points) and the m -th column of prismatic cells (red rectangular prisms), we imitate Equation (23), and then yield

$$\begin{pmatrix} K^{i+1,j+1} & \dots & K^{i+1,j+\Delta m} & \dots & K^{i+1,j+n_y} \\ \vdots & \ddots & \vdots & \ddots & \vdots \\ K^{i+\Delta q,j+1} & \dots & K^{i+\Delta q,j+\Delta m} & \dots & K^{i+\Delta q,j+n_y} \\ \vdots & \ddots & \vdots & \ddots & \vdots \\ K^{i+n_y,j+1} & \dots & K^{i+n_y,j+\Delta m} & \dots & K^{i+n_y,j+n_y} \end{pmatrix} \begin{pmatrix} \rho_{j+1} \\ \vdots \\ \rho_{j+\Delta m} \\ \vdots \\ \rho_{j+n_y} \end{pmatrix} = \begin{pmatrix} d_{i+1} \\ \vdots \\ d_{i+\Delta q} \\ \vdots \\ d_{i+n_y} \end{pmatrix} \quad (24)$$

Or,

$$\tilde{G}_{q,m} \tilde{\rho}_m = \tilde{d}_q \quad (25)$$

where $\tilde{G}_{q,m}$ is the sensitivity matrix for the Line–Line survey scheme, $\tilde{\rho}_m$ is the density vector for the m -th column prismatic cells, \tilde{d}_q is the observation vector due to the

m -th column prismatic cells on the q -th survey line, $i = (q - 1) \times n_x + (t - 1) \times N_d$, and $j = (m - 1) \times n_x + (n - 1) \times N_d$.

According to Equations (18) and (21), any observation point P on the q -th survey line and any prismatic cell Q in the m -th column can be shifted by a step of Δq and Δm along the X - and Y -axes, respectively, such as $\Delta q = 1$ and $\Delta m = 1$, yielding

$$K^{i+1,j+1} = K^{i+2,j+2} = \dots = K^{i+\Delta q,j+\Delta q} = \dots = K^{i+\Delta m,j+\Delta m} = K^{i+n_y,j+n_y} \tag{26}$$

So, it is found that the main diagonal elements of $\widetilde{G}_{q,m}$ have the same value. Or, $\Delta q = 1$ and $\Delta m = 2$:

$$K^{i+1,j+2} = K^{i+2,j+3} = \dots = K^{i+\Delta q,j+\Delta q+1} = \dots = K^{i+\Delta m,j+\Delta m+1} = K^{i+n_y-1,j+n_y} \tag{27}$$

Similarly, for other diagonals of $\widetilde{G}_{q,m}$, their elements have the same value. Therefore, $\widetilde{G}_{q,m}$ can be written as

$$\widetilde{G}_{q,m} = \begin{pmatrix} a_0 & a_1 & \dots & \dots & a_{n_y-1} \\ a_{-1} & a_0 & a_1 & & \vdots \\ \vdots & a_{-1} & a_0 & \ddots & \vdots \\ \vdots & & \ddots & \ddots & a_1 \\ a_{1-n_y} & \dots & \dots & a_{-1} & a_0 \end{pmatrix} \tag{28}$$

where $[a_0, a_{-1}, a_{-2}, \dots, a_{1-n_y}]^T$ and $[a_0, a_1, a_2, \dots, a_{n_y-1}]$ correspond to the first column and the first row of $\widetilde{G}_{q,m}$, respectively. $\widetilde{G}_{q,m}$ can be expressed with $2n_y - 1$ elements.

According to the definition of the Toeplitz matrix [77], $\widetilde{G}_{q,m}$ is a Toeplitz matrix (see Figure 7), which is also closely related to the Fourier series. The product of the matrix $\widetilde{G}_{q,m}$ and the vector $\widetilde{\rho}_m$ can be written as

$$\widetilde{G}_{q,m}\widetilde{\rho}_m = \mathcal{F}\left(F(\widetilde{a}^T) \cdot \mathcal{F}\left(\begin{pmatrix} \widetilde{\rho}_m \\ 0 \end{pmatrix}\right)\right) \tag{29}$$

where \mathcal{F} and F represent the Fourier transform and inverse Fourier transform, respectively; the part \widetilde{a} that needs to be stored for $\widetilde{G}_{q,m}$ is

$$\widetilde{a} = \left\{ [a_0, a_1, a_2, \dots, a_{n_y-1}] \quad 0 \quad \mathcal{F}([a_{-1}, a_{-2}, \dots, a_{1-n_y}]) \right\} \tag{30}$$

Similar to Equation (24), the relationship between other survey lines and other column prismatic cells can be constructed. As shown in Figure 6, we take the t -th layer observation points and the corresponding n -th layer prismatic cells of the 3D interpretation model as the Layer–Layer survey scheme. Mimicking Equations (23), (24), and (28), the sensitivity matrix $G_{t,n}$ for the Layer–Layer survey scheme can be written in matrix form with the submatrices $\widetilde{G}_{q,m}$, which are the sensitivity matrices of the Line–Line survey schemes:

$$G_{t,n} = \begin{pmatrix} \widetilde{G}_{1,1} & \widetilde{G}_{1,2} & \dots & \dots & \dots & \widetilde{G}_{1,n_y} \\ \widetilde{G}_{2,1} & \widetilde{G}_{2,2} & & & & \vdots \\ \vdots & & \ddots & \ddots & & \vdots \\ \vdots & & & \widetilde{G}_{q,m} & & \vdots \\ \vdots & & & & \ddots & \widetilde{G}_{n_y-1,n_y} \\ \widetilde{G}_{n_y,1} & & \dots & \widetilde{G}_{n_y,n_y-1} & & \widetilde{G}_{n_y,n_y} \end{pmatrix} \tag{31}$$

According to the extension translational equivalence technique and the definition of the block–Toeplitz–Toeplitz–block (BTTB) matrix [77], $G_{t,n}$ is a BTTB matrix (also a kind of Toeplitz-like matrix, see Figure 7). Therefore, the number of kernel functions that need to be

stored for the sensitivity matrix G of the traditional survey scheme based on the extension translational equivalence technique is

$$N_G^4 = N_m \times N_d = (2n_x - 1) \times (2n_y - 1) \times n_z \times 2 \tag{32}$$

Equation (28) is suitable for rectangular survey grids, and Equation (31) is suitable for square survey grids. In fact, by expanding the observation data matrix into a square matrix using zero matrices, Equation (28) can also be used to achieve rapid forward modeling of gravity fields for rectangular survey grids.

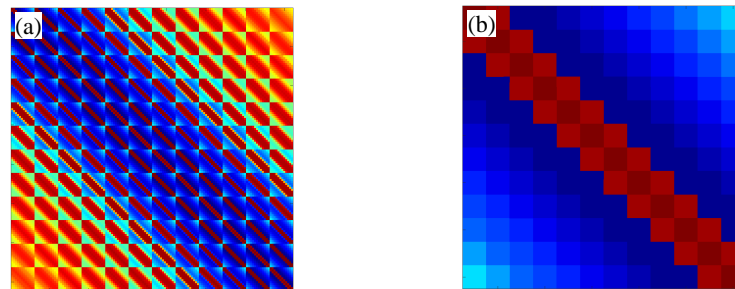


Figure 7. The diagrammatic sketch of sensitivity matrix g_{xx} of one-layer observation points is due to single-layer prismatic cells. (a) G_{t,n_i} ; (b) $\tilde{G}_{q,m}$.

The sensitivity matrix G of the traditional survey scheme is composed of single-layer observation points ($t = 1$) due to the multi-layer prismatic cells of the 3D interpretation model. According to Equations (1) and (31), the sensitivity matrix G is composed of several $G_{t,n}$ submatrices:

$$G = \begin{bmatrix} G_{1,1} & G_{1,2} & \cdots & G_{1,n} & \cdots & G_{1,n_z} \end{bmatrix} \tag{33}$$

For the equidimensional inversion survey scheme shown in Figure 3b, the sensitivity matrix G is composed of several $G_{t,n}$ matrices:

$$G = \begin{pmatrix} G_{1,1} & G_{1,2} & \cdots & \cdots & G_{1,n_z} \\ G_{2,1} & G_{2,2} & \cdots & & \vdots \\ \vdots & \vdots & G_{t,n} & \ddots & \vdots \\ \vdots & & \ddots & \ddots & G_{n_t-1,n_z} \\ G_{n_t,1} & \cdots & \cdots & G_{n_t,n_z-1} & G_{n_t,n_z} \end{pmatrix} \tag{34}$$

4. Multilevel Algorithm

The overall idea of the multilevel method follows the classical multigrid method [16], such as the multilevel method implementation process described by Español and Kilmer [68]. Based on the rapid forward modeling algorithm of gravity fields proposed in this article, this section details multilevel inversion of large-scale gravity and tensor gravity data.

4.1. Basic Framework

Following Español and Kilmer [68], Sima et al. [78], and Yao et al. [24], a new 3D inversion of large-scale gravity and tensor gravity data based on the multilevel method is introduced by defining a sequence of sensitivity matrices of decreasing size based on Equation (1) to obtain faster solvers.

$$G^k m^k = d^k, \quad 0 \leq k \leq n_{level} \tag{35}$$

where the superscript k denotes the k -th level, and $k = 0$ and $k = n_{level}$ correspond to the finest and coarsest levels, respectively. In particular, the 3D interpretation model is constructed using $n_x = n_y = 2^{n_{max}}$ and $n_{level} \leq n_{max}$ as constraints in the gravity forward/inversion.

The restriction operator R and the interpolation operator P define the transitions from finer to coarser grids and vice versa. The transformation between two neighboring levels is defined by

$$G^{k+1} = R^k G^k P^k \quad (36)$$

4.2. Haar Decomposition

Since the Haar wavelet has the advantage of being able to preserve the Toeplitz matrix structure between two neighboring levels, this study uses the Haar wavelet operator to replace R and P operators:

$$W^T = \frac{1}{\sqrt{2}} \begin{pmatrix} 1 & 1 & 0 & 0 & \dots & \dots & 0 & 0 \\ 0 & 0 & 1 & 1 & \dots & \dots & 0 & 0 \\ \vdots & \vdots & \vdots & \vdots & \ddots & \ddots & \vdots & \vdots \\ 0 & 0 & 0 & 0 & \dots & \dots & 1 & 1 \\ 1 & -1 & 0 & 0 & \dots & \dots & 0 & 0 \\ 0 & 0 & 1 & -1 & \dots & \dots & 0 & 0 \\ \vdots & \vdots & \vdots & \vdots & \ddots & \ddots & \vdots & \vdots \\ 0 & 0 & 0 & 0 & \dots & \dots & 1 & -1 \end{pmatrix} = \begin{bmatrix} W_1^T \\ W_2^T \end{bmatrix} \quad (37)$$

Then, our problem $Gm = d$ can be written in the wavelet domain as

$$\overline{G}\overline{m} = \overline{d} \quad (38)$$

where W and W^T are Haar wavelet transform pairs, then $\overline{G} = W^T G W$, $\overline{m} = W^T m$, and $\overline{d} = W^T d$.

In this study, Equation (38) can be split into several block matrices by using W_1 and W_2 to obtain the following problem:

$$\begin{bmatrix} \overline{G}_{11} & \overline{G}_{12} \\ \overline{G}_{21} & \overline{G}_{22} \end{bmatrix} \begin{bmatrix} \overline{m}_1 \\ \overline{m}_2 \end{bmatrix} = \begin{bmatrix} \overline{d}_1 \\ \overline{d}_2 \end{bmatrix} \quad (39)$$

where $\overline{G}_{ij} = W_i^T G W_j$, $\overline{m}_i = W_i^T m$, and $\overline{d}_i = W_i^T d$, for $i, j = 1, 2$. \overline{G}_{ij} can be proved to be typical Toeplitz-like matrices, as by Equation (28); for convenience, G could be expressed in matrix form as follows:

$$G = \begin{bmatrix} s_0 & s_{-1} & s_{-2} & \dots & s_{-(o-1)} \\ s_1 & s_0 & s_{-1} & \dots & s_{-(o-2)} \\ s_2 & s_1 & s_0 & \dots & s_{-(o-3)} \\ \vdots & \vdots & \vdots & \ddots & \vdots \\ s_{o-1} & s_{o-2} & s_{o-3} & \dots & s_0 \end{bmatrix} \quad (40)$$

Here, $s = (s_{-(o-1)}, \dots, s_{-1}, s_0, s_1, \dots, s_{o-1})^T$ is a Toeplitz vector of G . According to Lemma 8.5.3 [79], we have

$$\text{vec}(W_i^T G W_j) = (W_i^T \otimes W_j) \text{vec}(G) \quad (41)$$

where $E \otimes F$ denotes the Kronecker product of E and F , and $\text{vec}(E)$ unstacks the matrix E by columns to produce a column vector. Since Toeplitz matrices are circulant matrices, we use only two columns of G to generate the Toeplitz vector \overline{s} of \overline{G} . Then, Equation (41) can be rewritten in MATLAB notation as

$$\begin{aligned} \overline{s} &= (\varphi_i^T \otimes W_j) \text{vec}(G(:, 1:2)) \\ &\equiv (\varphi_i^T \otimes W_j) \text{vec}([s; s([2, 1:m-1])^T]) \\ &\equiv (\varphi_i \otimes W_j^T) \text{vec}([s; s([2, 1:m-1])^T]) \end{aligned} \quad (42)$$

where φ_i is the wavelet basis of the operator W_i . Therefore, \bar{G}_{ij} can be obtained using the Toeplitz vector s of G directly, which avoids storing the kernel matrices at each level of the multilevel inversion. Equation (42) is more concise than the solution to the computational issue in the paper of Español and Kilmer [68].

4.3. Algorithm Details

To solve for \bar{m}_1 from the first block equation of Equation (39), we have

$$\bar{G}_{11}\bar{m}_1 = \bar{d}_1 - \bar{G}_{12}\bar{m}_2 \quad (43)$$

While \bar{m}_2 is unknown, we try to find an approximation of \bar{m}_1^* to replace \bar{m}_1 by using pre-smoothing inversion. Then, Equation (43) can be rewritten as

$$\bar{G}_{11}\bar{m}_1^* = \bar{d}_1 \quad (44)$$

Equation (44) is suitable for solving the pre-smoothing problem and the coarsest grid correction problem defined in Español and Kilmer [68]. To recover this density contrast distribution with depth resolution, we solved a regularized problem:

$$\min_{\bar{m}_1^*} \left\{ \left\| W_d (\bar{G}_{11}\bar{m}_1^* - \bar{d}_1) \right\|_2^2 + \lambda \left\| W_z W_m (\bar{m}_1^* + \bar{m}_{1,ref}) \right\|_2^2 \right\} \quad (45)$$

where $\bar{m}_{1,ref}$ is the wavelet domain reference model, updated in real time during the inverse iterations.

To solve for \bar{m}_2 from Equation (39), according to Equation (44), we have

$$\begin{bmatrix} \bar{G}_{12} \\ \bar{G}_{22} \end{bmatrix} \bar{m}_2 = \begin{bmatrix} \bar{d}_1 \\ \bar{d}_2 \end{bmatrix} - \begin{bmatrix} \bar{G}_{11} \\ \bar{G}_{21} \end{bmatrix} \bar{m}_1^* \quad (46)$$

This step is called residual correction [68]. To solve this problem, Equation (46) is regularized by minimizing the Tikhonov functional to reduce the uncertainties associated with estimating geophysical variables, which then yields

$$\min_{\bar{m}_2} \left\{ \left\| W_d \left(\begin{bmatrix} \bar{G}_{12} \\ \bar{G}_{22} \end{bmatrix} \bar{m}_2 - \left(\begin{bmatrix} \bar{d}_1 \\ \bar{d}_2 \end{bmatrix} - \begin{bmatrix} \bar{G}_{11} \\ \bar{G}_{21} \end{bmatrix} \bar{m}_1^* \right) \right) \right\|_2^2 + \lambda \left\| W_z W_m (\bar{m}_2 + \bar{m}_{2,ref}) \right\|_2^2 \right\} \quad (47)$$

where $\bar{m}_{2,ref}$ is a wavelet domain reference model that is updated in real time during inverse iterations.

Following Español and Kilmer [68], Sima et al. [78], and Yao et al. [24], according to Equations (45) and (47), a new multilevel algorithm for 3D inversion of gravity/tensor gravity data is as specifically in Algorithm 1.

The Haar wavelet of multilevel inversion acts only in the horizontal direction of the interpretation model to distinguish between neighboring anomaly sources but not in the vertical direction of the 3D interpretation model. Due to algorithmic stability and smooth results, Occam's-style algorithms are used to solve Equations (45) and (47). The RRCG is the most widely used solver in focusing inversion and can obtain better depth resolution [55,80]. Considering the above two points, following Zhdanov [81,82], the RRCG algorithm is used as the solver for the multilevel algorithm in this paper. In order to meet the needs of comparison, Occam's inversion and multilevel inversion are utilized for comparative analysis in subsequent model experiments and field examples.

In Algorithm 2, n is the number of inversion iterations, and a series of diagonal weight matrices are defined as follows: $W_d = \text{diag}(GG^T)^{1/2}$, $W_m = \text{diag}(G^T G)^{1/2}$, the minimum support functional $W_e = \text{diag}((m - m_{ref})^2 + e^2)^{-1/4}$, and e is a very small positive number, especially in this paper, where $e = 0.015$.

Algorithm 1: Multilevel algorithm for 3D inversion of gravity/tensor gravity data: 3DML algorithm

Require: G^i, d^i, m_{ref}^i

Ensure: m^i

- 1: **if** $i = n$
 - 2: $m^i =$ solve Equation (42), in coarsest-grid level
 - 3: **else**
 - 4: **if** $i \neq 1$
 - 5: $m_{pre}^i =$ solve Equation (42), in pre-smoothing step
 - 6: $r_{new}^i = d^i - G_{11}^i m_{pre}^i$
 - 7: $\bar{d}^{i+1} = W_1^T r_{new}^{i+1}$
 - 8: **elseif** $i = 1$
 - 9: $m_{pre}^i = 0, m_{ref}^{i+1} = 0, \bar{d}^{i+1} = W_1^T d^i$
 - 10: **end**
 - 11: $\bar{m}_{ref}^i = W_1^T (m_{ref}^i + m_{pre}^i)$
 - 12: $\bar{G}_{11}^i = W_1^T G_{11}^i W_1$
 - 13: $\bar{m}_1^{i+1} = 3DML(\bar{G}_{11}^i, \bar{d}^{i+1}, \bar{m}_{ref}^i)$
 - 14: $\bar{m}_{ref}^i = W_1^T (m_{ref}^i + W_1 \bar{m}_1^{i+1})$
 - 15: $m_{new}^i = m_{pre}^i + W_1 \bar{m}_1^{i+1}$
 - 16: $\bar{m}_2^i =$ solve Equation (44), for residual correction step
 - 17: $m^i = m_{new}^i + W_2 \bar{m}_2^i$
 - 18: **end**
-

Algorithm 2: The algorithm of the RRCG method

Require: G, d, m_{ref}

Ensure: m_{n+1}

- 1: $r_n^w = G_w(m_n^{w_n}) - d^w = W_d G (W_m^{-1} W_{en}^{-1} m_n^{w_n}) - W_d d$
 - 2: $I_{w_n}^{\alpha_n} = I_{w_n}^{\alpha_n}(m_n^{w_n}) = G_w^T r_n^w + \alpha (m_n^{w_n} - m_{ref}^{w_n})$
 - 3: $\beta_n^{\alpha_n} = \|I_{w_n}^{\alpha_n}\|^2 / \|I_{w_{(n-1)}}^{\alpha_{n-1}}\|^2$
 - 4: $\tilde{I}_{w_n}^{\alpha_n} = I_{w_n}^{\alpha_n} + \beta_n^{\alpha_n} \tilde{I}_{w_{n-1}}^{\alpha_{n-1}}, \tilde{I}_{w_0}^{\alpha_0} = I_{w_0}^{\alpha_0}$
 - 5: $K_n^{\alpha_n} = (\tilde{I}_{w_n}^{\alpha_n})^T I_{w_n}^{\alpha_n} / [(\tilde{I}_{w_n}^{\alpha_n})^T (G_w^T G_w + \alpha I) \tilde{I}_{w_n}^{\alpha_n}]$
 - 6: $m_{n+1}^{w_n} = m_n^{w_n} - K_n^{\alpha_n} \tilde{I}_{w_n}^{\alpha_n}, m_{n+1} = W_m^{-1} W_{en}^{w_n} m_{n+1}^{w_n}$
 - 7: $m_{n+1}^{w_{n+1}} = W_m W_{e(n+1)} m_{n+1}, s_{n+1}^{w_{n+1}} = (m_{n+1}^{w_{n+1}} - m_{ref}^{w_{n+1}})$
 - 8: $\gamma = \|s_{n+1}^{w_{n+1}}\|^2 / \|s_n^{w_n}\|^2$
 - 9: $\alpha_{n+1} = \alpha_n$, **if** $\gamma \leq 1$, and $\alpha_{n+1} = \alpha_n / \gamma$, **if** $\gamma > 1$
 - 10: $\alpha'_{n+1} = q \alpha_{n+1}, q < 1, \|r_n^w\|^2 - \|r_{n+1}^w\|^2 < 0.01 \|r_n^w\|^2$
-

5. Calculation Accuracy of the Rapid Forward Algorithm

The following 3D interpretation model is constructed to verify the correctness of the rapid algorithm proposed in this paper. There is an anomalous body with a size of $300 \text{ m} \times 300 \text{ m} \times 300 \text{ m}$ and a density of 0.3 g/cm^3 . Its roof and bottom depths are 500 m and 800 m, respectively. The projection of the centroid of the anomalous body on the ground is taken as the origin of the Cartesian coordinate system; n_x, n_y , and n_z are 40, 40, and 30, with a 50 m grid spacing, respectively. The number of observation points is

$40 \times 40 = 1600$, and the observation height is 50 m above the ground surface. The 3D earth model is discretized into $40 \times 40 \times 30 = 48,000$ cubic cells with a side length of 50 m. The forward results of the rapid algorithm are shown in Figure 8.

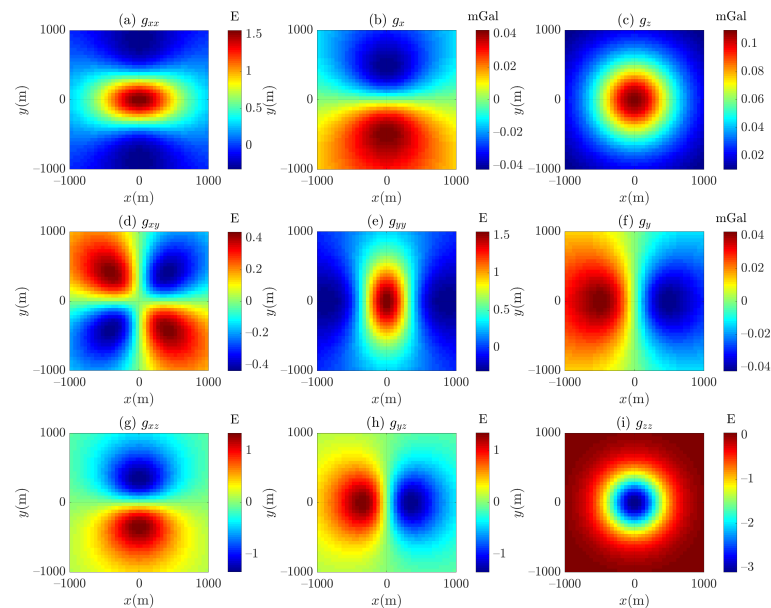


Figure 8. Rapid algorithm's forward results for different components (a) g_{xx} , (b) g_x , (c) g_z , (d) g_{xy} , (e) g_{yy} , (f) g_y , (g) g_{xz} , (h) g_{yz} , and (i) g_{zz} .

Figure 9 shows the relative error of the forward results between the rapid algorithm and the analytical solution proposed by Li and Chouteau [13]. It can be seen that the forward results are very smooth with no ambiguity points and are close to zero, which is several orders of magnitude smaller than other algorithms. The rapid algorithm proposed in this paper has exceptionally high precision.

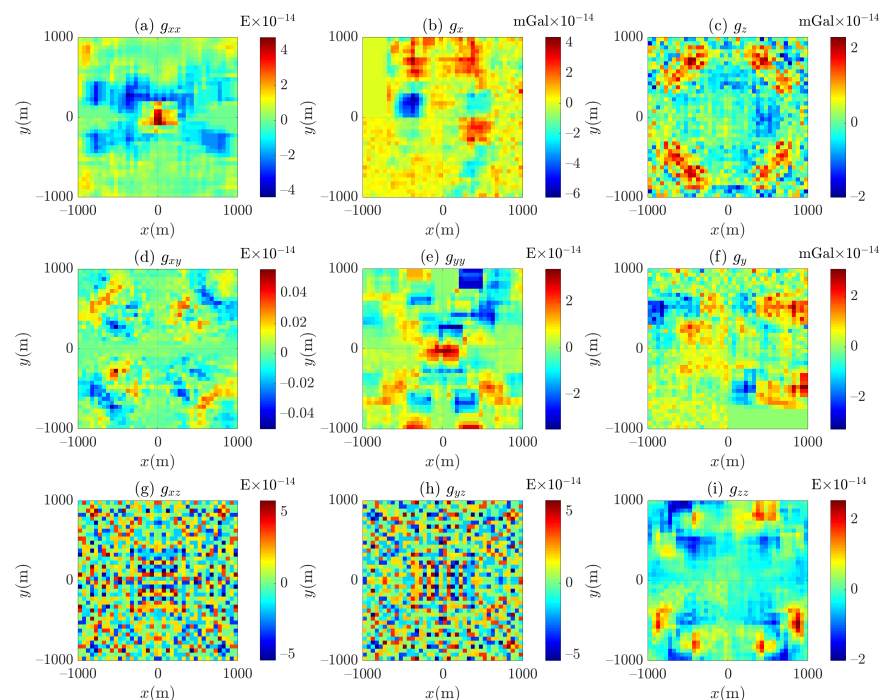


Figure 9. The relative error of forward results between the rapid algorithm and analytical solution [13] for different components (a) g_{xx} , (b) g_x , (c) g_z , (d) g_{xy} , (e) g_{yy} , (f) g_y , (g) g_{xz} , (h) g_{yz} , and (i) g_{zz} . E stands for Eotvos, which is standard for characterising how sensitive different gravity gradiometers ($1 \text{ Eotvos} = 10^{-9} \text{ s}^{-2}$).

6. Performance of the Rapid Forward Algorithm

A series of different-sized models, with a square grid ($n_x \equiv n_y$) and cubic cells, were constructed to verify the effectiveness of the rapid algorithm proposed in this paper by comparing it with the other two algorithms, those of the traditional analytical method and the equivalent geometric framework, implemented according to the works of Li and Chouteau [13] and Yao et al. [24]. The parameters n_x , n_y , and n_z of these models were set to exponential powers of 2. The square observation grids and corresponding geophysical models were constructed with integer powers from 2 to 9, respectively. A total of 36 models were constructed, as shown in Figures 10 and 11. The smallest model had n_x , n_y , and n_z of 8, 8, and 8 ($N_d = 64$ and $N_m = 256$), respectively, while the largest model had n_x , n_y , and n_z of 256, 256, and 32 ($N_d = 65,536$ and $N_m = 2,097,152$), respectively. The densities of cubic cells in these models are set to a random value to represent complex geological structures.

We then compared these forward modeling algorithms' time and peak memory consumption for g_z with different-sized 3D models. On an Ubuntu 18.04 LTS operating system with an Intel® Xeon® Gold 5117 CPU @2.00 GHz and 120 GB of memory, the pcode function in MATLAB 2018a was used to compile the codes of the forward modeling algorithms into P-code files. The following computation times and peak memory usage are statistical averages obtained by averaging five runs. With OpenMP 56 threads and MATLAB mixed programming methods, the rapid algorithm achieved a better acceleration factor. Several models where the logarithm of the observation grid size was greater than nine were not computed because the computation time was too long.

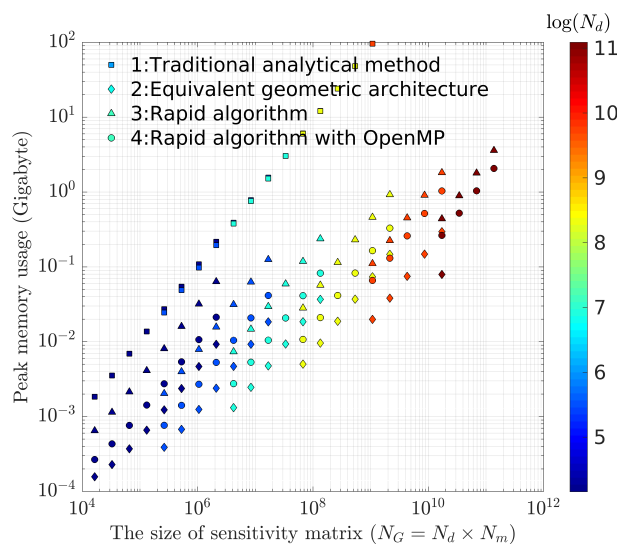


Figure 10. Peak memory usage to calculate g_z fields with different-sized models ($N_m = N_G/N_d$, $n_x \equiv n_y = \sqrt{\text{int}(N_d)}$, and $N_z = N_m/N_d$).

In Figure 10, if the color and the corresponding value N_G of the point are known, it can be determined that $N_m = N_G/N_d$, $n_x \equiv n_y = \sqrt{\text{int}(N_d)}$, and $N_z = N_m/N_d$. The same color markers have the same observation grid size. When comparing the same color markers among different algorithms, the log–log plot of the peak memory usage versus the size of the sensitivity matrix shows an excellent linear relationship. The peak memory usage of these algorithms increases sharply with model size. Due to the steepness of the slope, several data points overlap. The order of magnitude among the three algorithms is consistent with the number of kernel functions that need to be stored for the sensitivity matrix in Equations (6), (20), and (32). Because it holds fewer intermediate variables in memory, the rapid algorithm with OpenMP technologies consumes less memory than the rapid algorithm without OpenMP technologies. The same conclusion applies to the other components of gravitational fields.

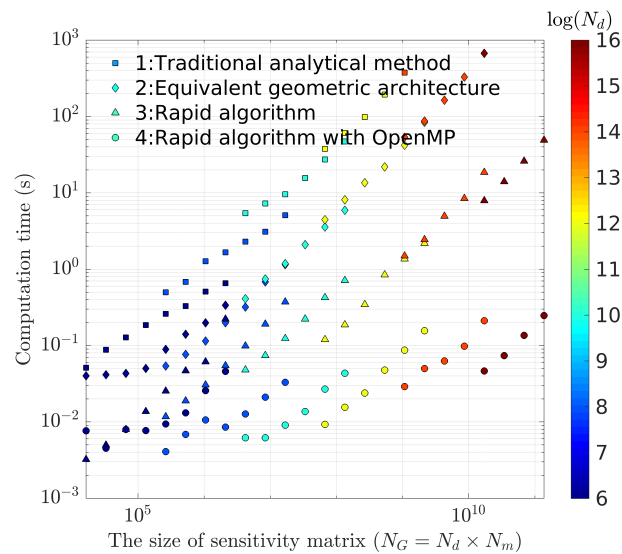


Figure 11. Calculation time obtained by performing g_z fields with different sizes of models.

As shown in Figure 11, when comparing different algorithms for the same color maker, the log–log plot of computation time versus model size shows an excellent linear relationship, and all curves increase dramatically with increasing model size. For the calculation times of different forward modeling algorithms, the traditional analytical method is the longest, which increases sharply with model size; the equivalent geometric architecture is about an order of magnitude smaller than the traditional analytical methods. According to the curves of different forward modeling algorithms, the traditional analytical methods are sharp, the equivalent geometric architecture is second, and the rapid algorithm is gentler than others. It is shown that the quick method has a remarkable capacity for acceleration, which increases with the model size. The rapid algorithm using OpenMP technology achieves two orders of magnitude more acceleration than the rapid algorithm using 56 threads. For other FTG components, the computational time is related to the computational complexity [13]. For large interpretation models, there is insufficient system memory when the peak memory usage is greater than the physical memory of the computing equipment. As a result, not all available virtual addresses of the MATLAB process could be mapped, significantly reducing computational efficiency and dramatically increasing computation time.

7. The Verification of the RRCG Algorithm

To verify the correctness of the RRCG algorithm used in this paper, a set of synthetic models was constructed (see Figure 12). Each synthetic model consists of two cube anomaly sources of size $200\text{ m} \times 200\text{ m} \times 200\text{ m}$, with a residual density of 1.0 g/cm^3 . Furthermore, 32, 32, and 10 for n_x , n_y , and n_z , respectively, were present in the subsurface, with an observation point height of 25 m and an observation point spacing of 50 m. In this paper, all 2D images of observation data and 2D/3D slices of the models were plotted using MATLAB's `imagesc` and `slice` functions, respectively.

In Figure 12, the forward results are contaminated by zero-mean Gaussian noise with a standard deviation equal to 3% of the maximum peak-to-peak amplitude of the components, as shown in Figure 12a,c,e,g. The response of the anomaly sources is simulated at different depths. The deeper the source, the less it weighs in the gravity field. At this point, it is similar to the response generated by two anomalies with different densities. We moved the left anomaly sources downward at $\Delta z = 0, 100, 200,$ and 300 , as shown in Figure 13. Then, following the paper of Portniaguine and Zhdanov [37], the RRCG inversion was employed to invert noisy data, and the resulting figures are presented in Figure 13b,d,f,j.

As illustrated in Figure 12, with increasing depth the contribution of the left anomaly source gradually decreases until the gravity peak on the left side of Figure 12g is completely

absent at $\Delta z = 300$. A similar phenomenon is observed in the data residuals of the RRCG inversion. As the Δz increases, the left peak in the residual gradually fades, and, even at $\Delta z = 300$, both peaks disappear. Examining Figure 13b,d,f,j, it can be observed that at $\Delta z = 0$ and $\Delta z = 100$, the density value of the reconstructed density model is mainly influenced by the upper limit ($1.0 \text{ g}\cdot\text{cm}^{-3}$).

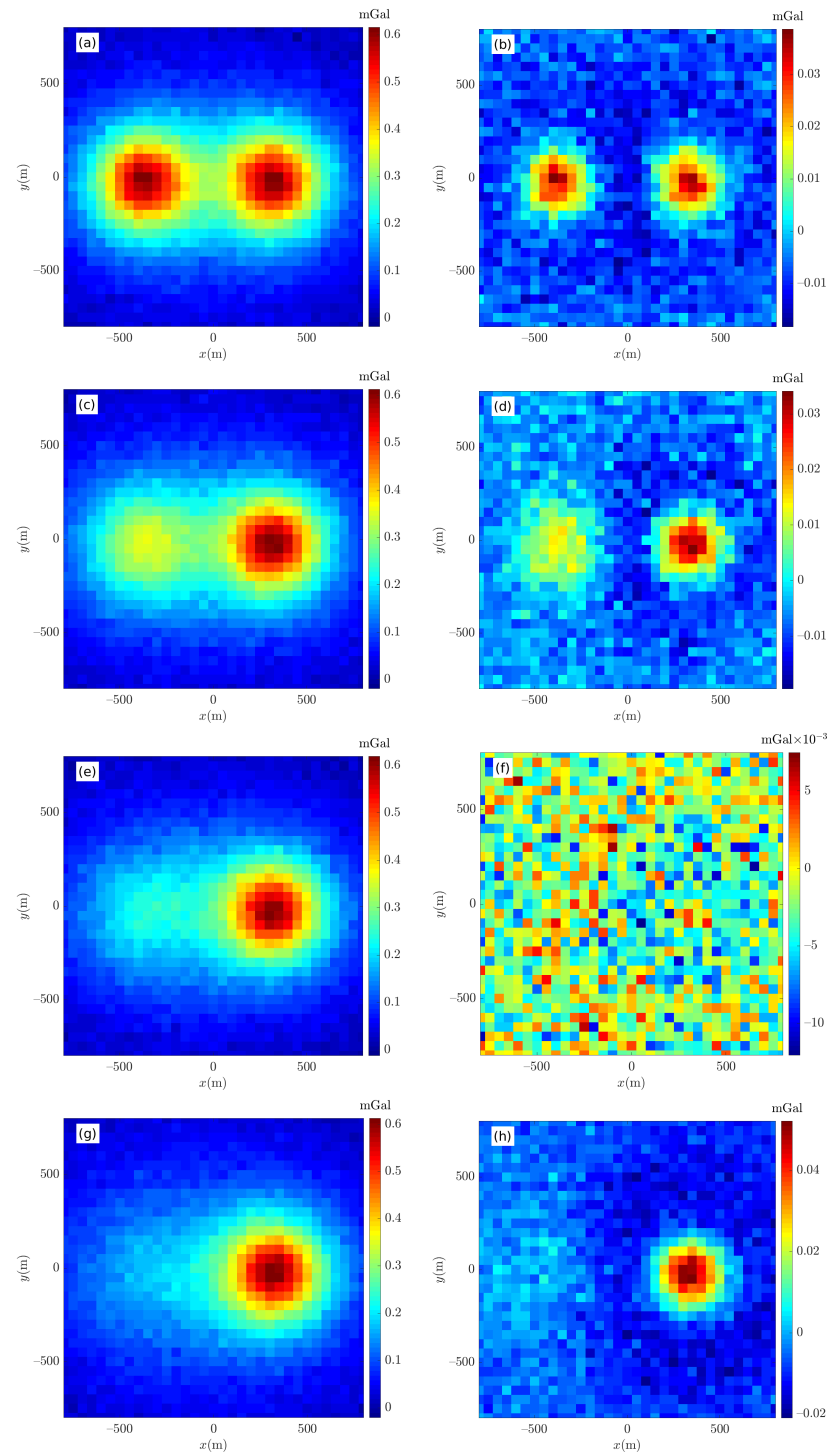


Figure 12. Gravity data. The first and second columns are noise-contaminated gravity data and residual data of the RRCG inversion, respectively. The columns from top to bottom are $\Delta z = 0, 100, 200,$ and 300 , respectively.

When $\Delta z = 200$ and 300 , the density value of the left reconstructed density model decreases significantly, which is speculated to be the reason for the disappearance of the peak value in Figure 12f,j. However, with the change in the gravity contribution of two adjacent anomalies, the reconstructed density model of the relatively strong anomaly source response obviously moves down. Conversely, the reconstructed density model of the relatively weak anomaly source response exhibits a significant upward shift ($\Delta z = 300$, with a tendency to shift outward, but still able to generally mark the location of the anomaly source). This experiment demonstrates that the RRCG algorithm is highly adaptive.

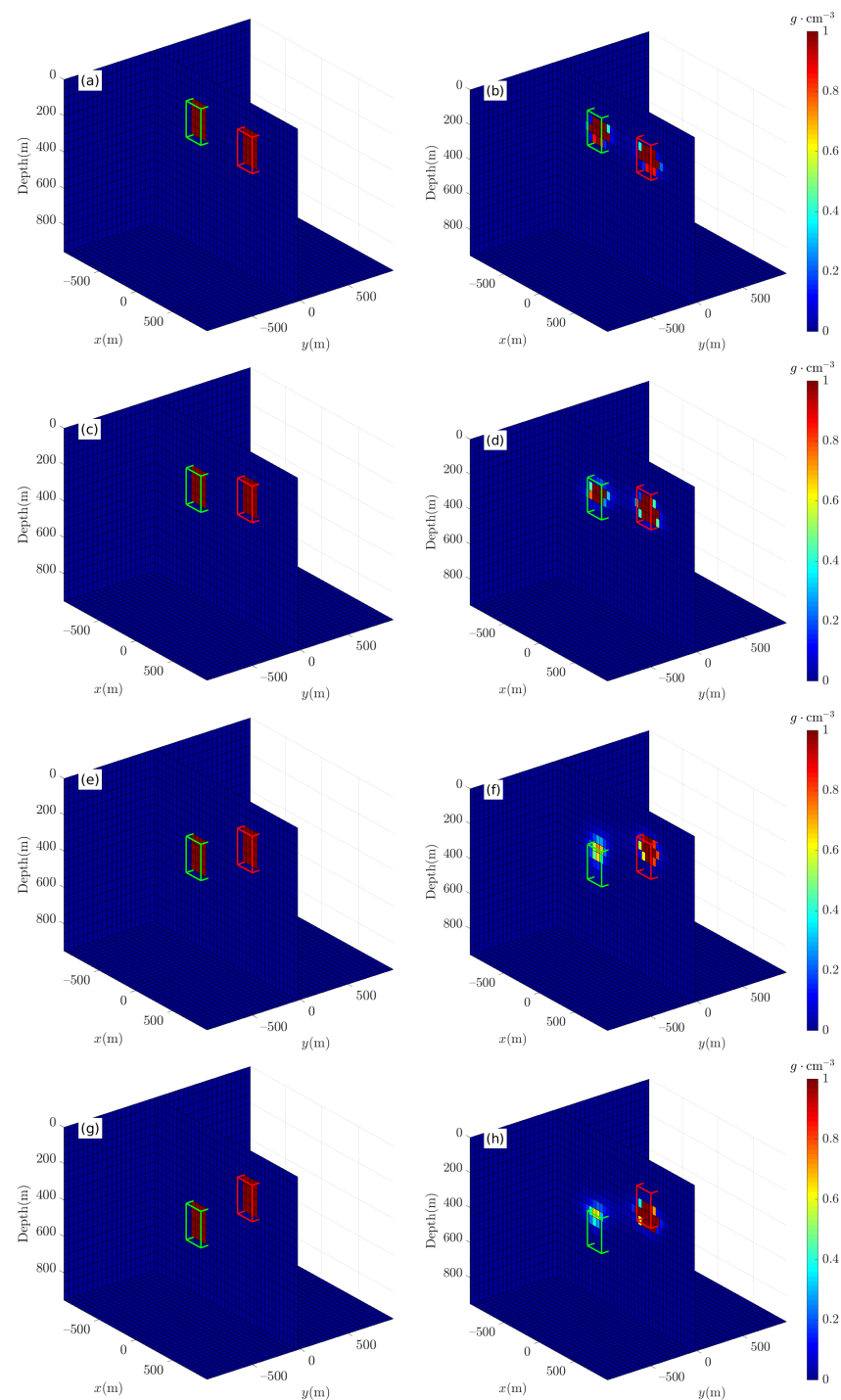


Figure 13. The slices of density models. The first and second columns represent forward and inversion models, respectively. The columns from top to bottom are $\Delta z = 0, 100, 200$, and 300 , respectively. $m_{min} = 0$ and $m_{max} = 1.0 \text{ g/cm}^3$.

8. Model Studies

To validate the principle of the multilevel inversion proposed in this paper, we inverted the noise-corrupted data in Figure 12a and compared them using Occam's inversion. In Figure 14, by following the paper about Occam's inversion [28,72], the decay index of the depth-weighting function $\beta = 1.8$. The flatness $a_x = 1$, $a_y = 1$, and $a_z = 1$ in the x , y , and z directions, respectively, and $a_s = 0.0005$. Readers are referred to Li and Oldenburg [28] for further details. The lower and upper bounds of the density constraint were set to 0 and 1.0 g/cm^3 , respectively. Following Zhdanov [81,82], the RRCG-based multilevel inversion had density constraints of lower and upper bounds by $m_{min} = 0$ and $m_{max} = 1.0 \text{ g/cm}^3$. Generally speaking, for 3D inversion of actual data, the upper and lower bound densities are determined by the lithology analysis of the survey area [55].

The inversion density slices were obtained using Occam's inversion, as shown in Figure 14. The density value of the inversion density contrast distribution decreases with increasing depth z , which makes it difficult to identify the basement of anomalous sources with the help of Occam's inversion result. Due to volume effects, this ultimately results in a 3D density distribution whose density values are far from reality [83].

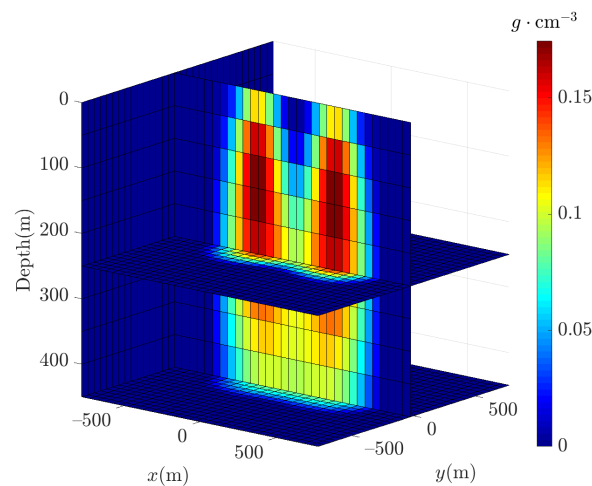


Figure 14. Inversion density slices obtained using Occam's inversion.

Figure 15 shows inversion density slices for multilevel inversion. The RRCG algorithm's overfocusing phenomenon leads to higher internal density values in the inversion density model for multilevel inversion [84]. Additionally, the kernel function decreases sharply with depth, resulting in lower density values at the top than those at the bottom. Compared to Occam's inversion results shown in Figure 14, the multilevel inversion results show a clear roof and floor in the depth direction of the model, demonstrating that the RRCG-based multilevel inversion method can better extract depth-resolved information; in the horizontal direction, compared with Occam's inversion results, in which distinguishing neighboring anomaly sources effectively is difficult, multilevel inversion results differentiate the two neighboring sources.

Occam's inversion is a smooth inversion, and its result and corresponding prediction data are also smooth. Due to the small range of the survey grid, the data residuals (see Figure 16a) have a random (similar) Gaussian noise distribution. The multilevel inversion solver is a focusing inversion solver, i.e., RRCG, so the inversion result is focused, which causes the residual to show two peaks above the anomaly, and the amplitude is larger than the residual of Occam, as shown in Figure 16b.

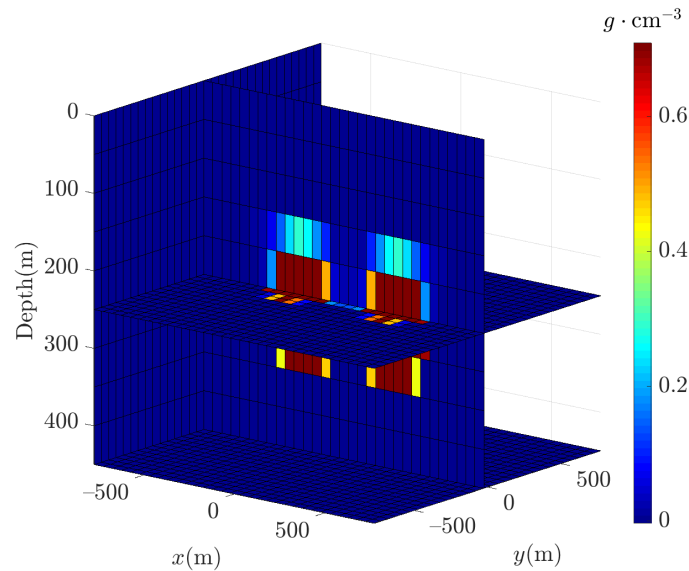


Figure 15. Inversion density slices obtained using multilevel inversion.

As shown in Figure 17, the data residuals from Occam's inversion are minimal and can be quickly stabilized (see Figure 16). For the multilevel inversion, the corresponding data misfit curves in different levels are significantly different due to the differences in the data used for the inversion processed by the Haar wavelet in different levels. For example, in Algorithm 1, there is no pre-smoothing inversion for $i = 1$, and, thus, there is no data misfit curve plotted in Figure 16; in the pre-smoothing inversion for $i = 2$, the part of the data extracted by the Haar wavelet for the inversion that is low-frequency has a large amount of energy, resulting in a large amplitude of the corresponding data misfit curve; in the coarse-grid correction for $i = 3$, the data misfit decays rapidly into a steady state with the inversion iteration, just like other levels of the inversion. Like other levels, the data misfit quickly decays to a steady state with the inversion iteration. Since the data to be corrected are in the high-frequency part, the residual correction manifests as a very small data misfit, consistent with that described in Algorithm 1.

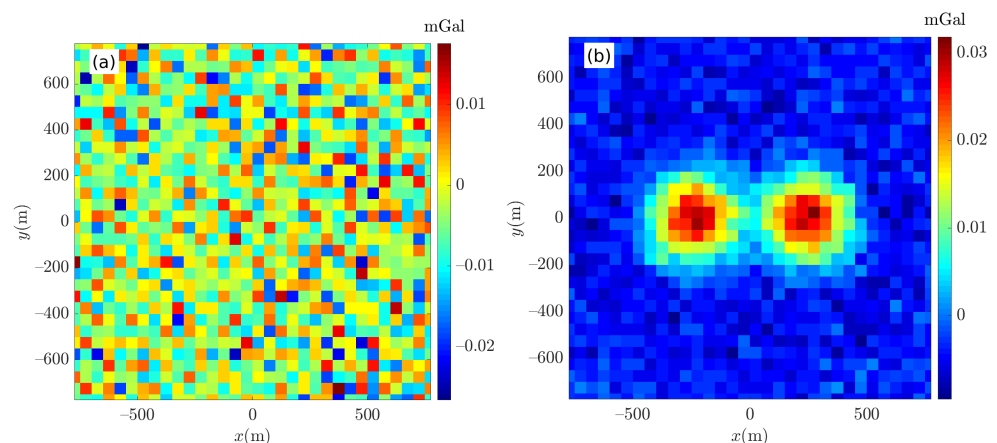


Figure 16. Residuals between observed and predicted data obtained by (a) Occam's inversion, and (b) multilevel inversion.

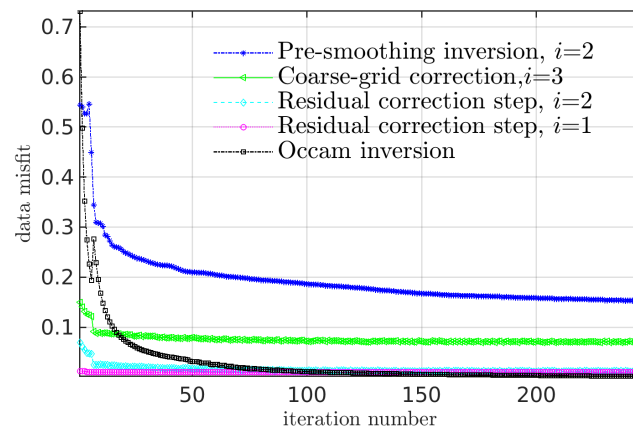


Figure 17. Data misfit obtained by Occam's and multilevel inversion.

Compared to the forward model in Figure 13a, it can be found that the inversion density model of multilevel inversion has a high degree of matching with the forward model. This indicates that compared multilevel inversion has a substantial advantage over an Occam's-style algorithm in both the depth resolution of extracted anomaly sources and the ability to distinguish neighboring anomaly sources. It also shows that the RRCC-based multilevel inversion proposed in this paper is correct. Under the same computing platform, Occam's inversion calculation in Figure 14 takes 329 s, while the multilevel inversion algorithm in this paper adopts the rapid forward calculation method, resulting in an inversion calculation time of only 27 s.

9. Sensitivity of Multilevel Inversion to Gaussian Noises

To verify the adaptability of the proposed algorithm to noise, we increased the noise level in Figure 12b from 3% to 8%, as shown in Figure 18a. Subsequently, the multilevel inversion algorithm was employed to obtain the reconstruction density model and the corresponding data residuals, as shown in Figure 18b,c.

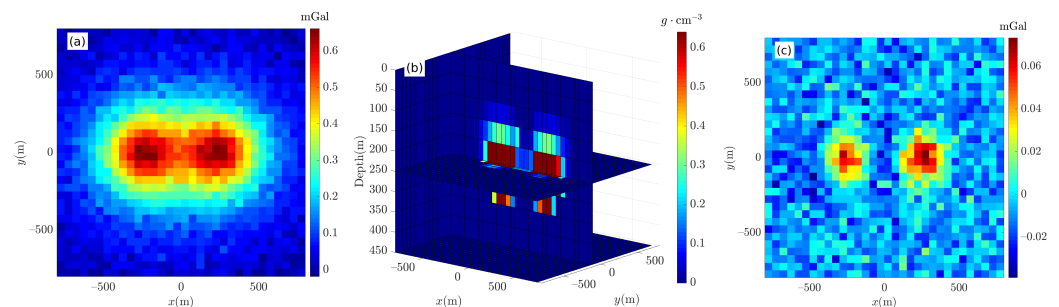


Figure 18. Example of multilevel inversion for noise-corrupted data (8%), (a) noise-corrupted data, (b) reconstructed density model, and (c) residual data.

Compared to the noise-corrupted data (3%) in Figure 12a, the noisy data (8%) in Figure 18a are more chaotic. However, as shown in Figures 15 and 18b, there is no discernible difference between the inversion results of the two noisy data sets (3% and 8%). The reconstruction density model derived from the noisy data (8%) shows some perturbation at its top and bottom. At the same time, an examination of Figures 17 and 19 shows that the amplitude of the fit curve of the inversion data with noise data (8%) is higher than 3%. Furthermore, in the subsequent correction inversion, the value of the data misfit does not tend to 0, which is also reflected in the corresponding data residual map of the two, as shown in Figures 16b and 18c. This demonstrates that the multilevel inversion method proposed in this paper can be applied to high-level noise data.

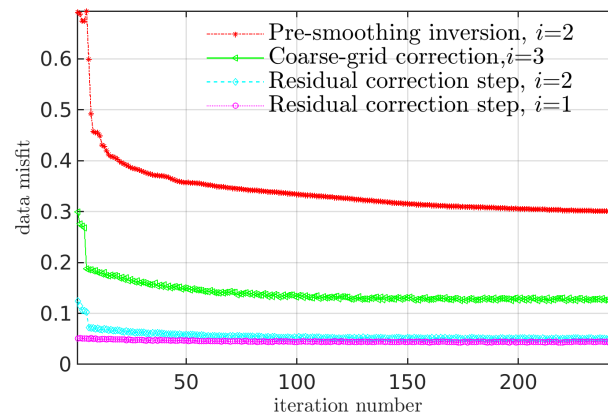


Figure 19. Data misfit obtained by multilevel inversion for noise-corrupted gravity data (8%).

The Haar wavelet was employed to divide the input data into two distinct categories: high-energy, low-frequency signals and low-energy, high-frequency noises, under the framework of multilevel inversion. Subsequently, the inversion algorithm proposed in this paper was used to process the low-frequency, high-energy signals of the data. This ensured that a better reconstruction model could be obtained. Finally, the low-energy, high-frequency noises were inverted in the subsequent residual correction. Due to the low amplitude of this portion of the signal, the use of the previous pre-smoothed inversion results as the reference model effectively eliminated the influence of low-energy, high-frequency noise on the inversion results. Nevertheless, these factors may result in the subsequent residual correction inversion becoming unstable.

10. Synthetic Gravity Data Experiment

To illustrate the performance of the rapid forward algorithm, we constructed massive surface gravity data using the SEG/EAGE salt model [85,86], which is one of the classic velocity salt dome models for seismic surveying research and was designed by SEG and EAGE. The salt model is available at https://s3.amazonaws.com/open.source.geoscience/open_data/seg_eage_models_cd/Salt_Model_3D.tar.gz (accessed on 6 January 2024) and comprises the 3D subsurface velocity model, model surface, and grid information, as shown in Figure 20a. The salt body was assumed to have a constant density contrast of -0.2 g/cm^3 . An interpretation model was discretized into $95,964,960 = 676 \times 676 \times 210$ cubic cells with a 20 m edge along the x , y , and z directions, respectively. A rectangular survey grid corresponding to the interpretation model was divided into $456,976 = 676 \times 676$ observation points, with a 20 m space-sampling interval and a 10 m observation height. Then, we used Occam's inversion and multilevel inversion to invert g_z data contaminated by zero-mean Gaussian noise with a standard deviation σ equal to 3% of the maximum peak-to-peak amplitude of the components, as shown in Figure 20.

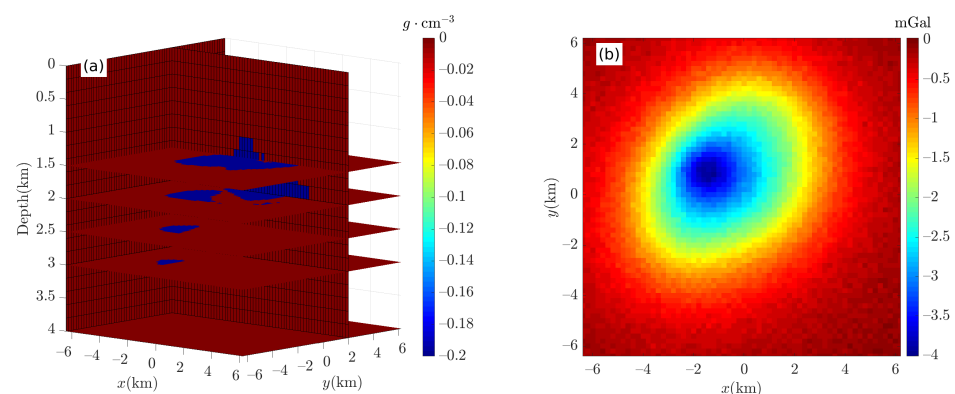


Figure 20. SEG/EAGE salt dome model (a) the forward model; (b) the forward result of g_z .

The upper and lower bounds of the density constraint for the RRCG-based multilevel inversion are set to 0.0 and -0.2 g/cm^3 , respectively. The parameters of Occam's inversion are: $\beta = 1.8$, $a_x = 1$, $a_y = 1$, $a_z = 1$, $a_s = 0.0005$, and $m_{min} = -0.20$ and $m_{max} = 0.05 \text{ g/cm}^3$.

Occam's inversion is a smooth inversion that results in smooth density variations between neighboring prismatic cells. As a result, density values are assigned to prismatic cells that do not have density values in the forward model (see Figure 20a). Since the gravity field results from the comprehensive reflection of underground geological structures, i.e., the volume effect [83], this leads to small density values in the 3D density contrast distribution obtained from Occam's inversion. Similar to Occam's inversion results in Figure 14, Occam's inversion results failed to effectively bring the depth resolution of the salt dome model in Figure 21.

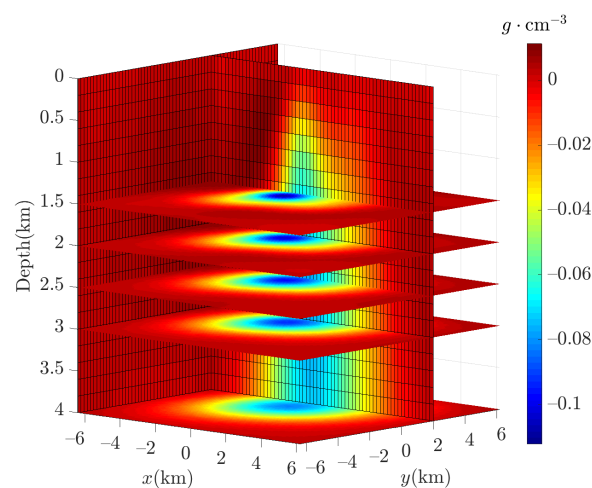


Figure 21. Result of inversion of g_z using Occam's inversion.

In Figure 22, the 3D density contrast distribution of the multilevel inversion g_z data has good depth resolution, and the density values at the roof and bottom follow a similar trend as in Figure 15. To meet the requirements to use Haar wavelets in the multilevel inversion for the field data, the taper2d function [87] was employed to perform a gradual tapering by applying a cosine function to the four borders of the 2D input matrix of the observation data to generate a new square matrix with a size of $n_x = n_y = 2^{n_{max}}$. At the end of the inversion process, the externally expanded data and models were removed to ensure that the final inversion results were consistent with actual data. However, this treatment can lead to some unstable bands at the boundaries of the data residuals, as shown in Figure 23a. Compared with the results of Occam's inversion, the multilevel inversion has a good convergence trend; however, due to the influence of the Haar wavelet, its data residuals are still significant in a small part of the region, which is consistent with its data mismatch curve, as shown in Figures 23 and 24.

Due to the lack of depth resolution of potential field data, it is difficult to reconstruct the vertical resolution in the inversion of physical properties, i.e., it is difficult to reconstruct the deep anomaly in the southwest of the salt model (e.g., the similar situation in the inversion of γ -dikes using Occam the article by Li and Oldenburg [28]), which, in turn, leads to the reconstruction results showing a "spindle shape". In effect, a "class" fault, stair, or step is formed at the edge of the geophysical model. This phenomenon represents a banded anomaly in the residual map of Occam's inversion. Compared to Occam's inversion results, the multilevel inversion results are more concentrated due to the overfocusing effect of the RRCG solver, resulting in the formation of a strip anomaly composed of multiple "peaks" in the residual map. However, the residual amplitude caused by these two is very small, which does not affect the convergence of the multilevel inversion.

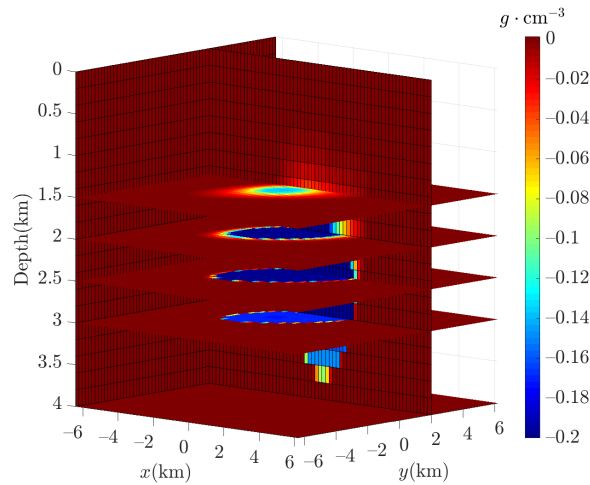


Figure 22. Result of inversion of g_z using multilevel inversion.

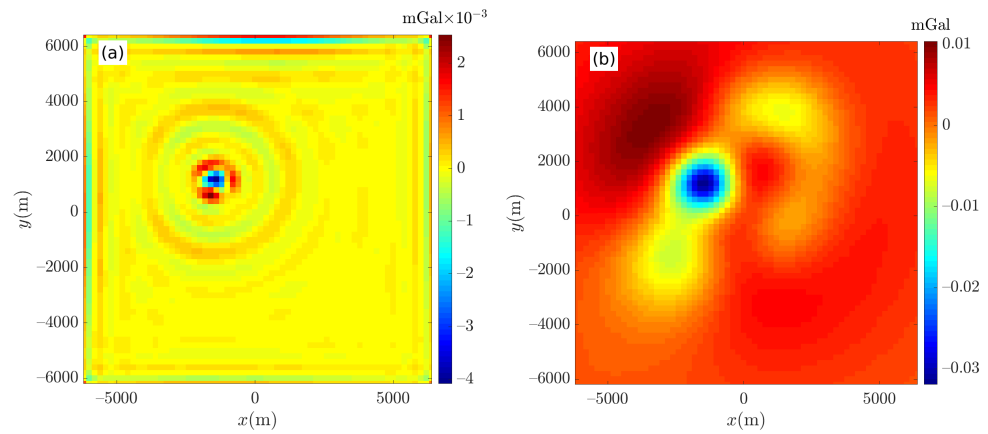


Figure 23. Residuals between observed and predicted data obtained by (a) Occam's inversion; (b) multilevel inversion.

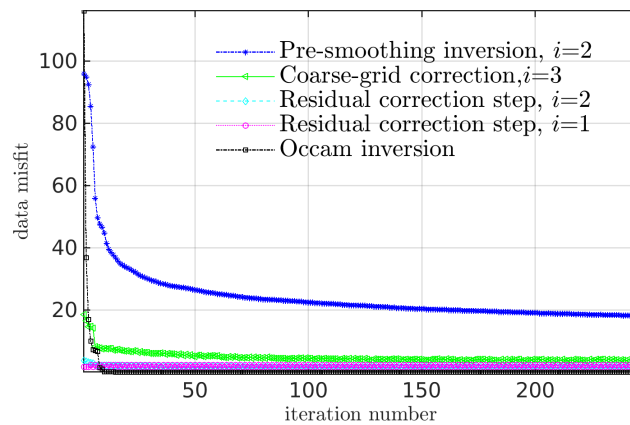


Figure 24. Data misfit obtained by Occam's and multilevel inversion.

For the salt dome model example (see Figure 20a), on the same computing platform, Occam's inversion calculation took 28,262 s. However, the multilevel inversion algorithm used the rapid forward calculation method proposed in this paper, resulting in a calculation time of only 1557 s.

11. Real Data Study

The survey area was located in the Quesnellia Region in British Columbia, Canada, a region famous for copper and gold porphyry deposits. Several gold and silver (plus copper, lead, and zinc) deposits have been mined in this area since 1884 [88–90]. The QUEST-South project was designed and managed by Geoscience BC in 2007, and its main exploration and mining area was the Quesnel Terrane [91]. It is a volcanic-arc terrane formed between the late Paleozoic and Mesozoic periods, and then merged into the western margin of the ancestral North American Craton through geological movements [92]. The porphyry copper-gold mineralization in the Quesnel Terrane is related to magmatic events, which are related to the late development of the terrane. Therefore, many experts and scholars have conducted extensive research on the bedrock geology of the terrane. For example, Mitchinson [91] and Sanchez et al. [93] successively evaluated the magnetic and electromagnetic data of the Quesnel Terrane, focusing on the intrusive rocks that serve as the host of porphyry copper deposits in the Quesnel Terrane, and completed the geological and structural interpretation of this area. To date, the alkaline porphyry deposits mined in the Quesnel block include Mount Milligan, Mount Polley, New Afton, and Copper Mountain deposits [91]. The region is covered by a thick layer of sand and gravel left behind by the glaciers. Airborne gravity surveys were used to identify potential targets and help understand the geology of this area [94,95].

The project is located between 547,500 m and 769,000 m easting and 5,427,500 m and 5,798,000 m northing and covers an area of 45,000 km² in south-central British Columbia that extends south of Williams Lake to the US border, as shown in Figure 25. It aims to provide comprehensive regional geochemical and geophysical information to local industry.

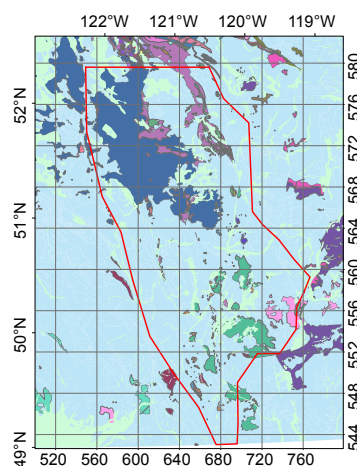


Figure 25. Survey area map. The red line corresponds to the QUEST-South geophysical survey, the light green blocks are Quaternary sedimentary strata, and the other colors are bedrock. Please see Erdmer and Cui [96] for details.

The field data are airborne gravity data that contain seven sub-blocks collected by Sander Geophysics in 2009 at a line spacing of 2000 m and corrected with a terrain correction and Bouguer correction applied by Geoscience BC at a density of 2.67 g/cm³ in a gridded format with a 500 m grid size [97], as shown in Figure 26. An interpretation model was discretized into 444 × 742 × 44 = 14,495,712 cubic cells in the x , y , and z directions. The length of the cubic cell edge is 500 m. A rectangular survey grid was divided into 444 × 742 = 329,448 observation points, with a 500 m space-sampling interval in both the x and y directions. Then, multilevel inversion and Occam's inversion were employed to invert the upward continued data using the rapid forward algorithm proposed in this paper. The parameters of Occam's inversion were $\beta = 1.8$, $a_x = 1$, $a_y = 1$, $a_z = 1$, $a_s = 0.0005$, and $m_{min} = -0.30$ and $m_{max} = 0.30$ g/cm³. The lower and upper bounds of the density constraint for the RRCG-based multilevel inversion were set to -0.40 and 0.40 g/cm³, respectively.

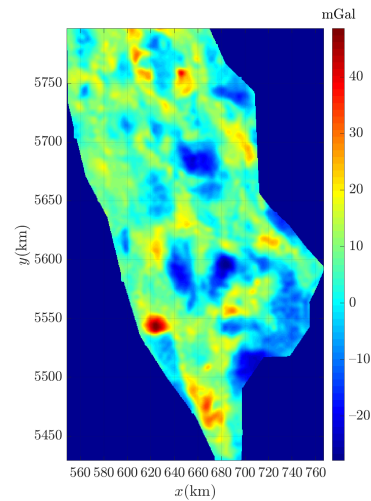


Figure 26. Residual gravity data provided by Sander Geophysics [97].

To facilitate further comparison, Mira Geoscience Limited [98] provided the inversion density contrast distribution (see Figure 27) using the UBC-GIF inversion code, which is based on an Occam's-style approach [28,72]. The position of the vertical density slice $z = [500 \text{ m}, 1300 \text{ m}, 2100 \text{ m}, 2900 \text{ m}, 3700 \text{ m}, 4500 \text{ m}]$. Due to the lack of depth resolution in surface gravity data [28] and the limitations of an Occam's-style algorithm in recovering depth resolution, the density contrast distribution map becomes progressively less clear as the depth z increases.

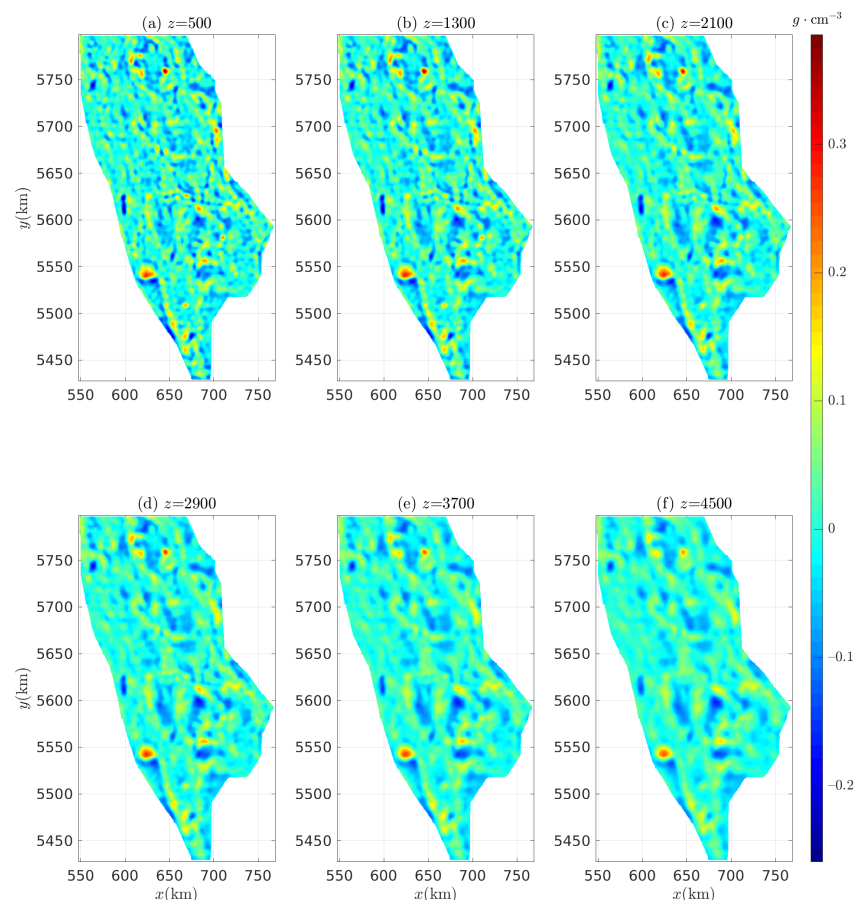


Figure 27. Inversion density distributions provided by Mira Geoscience Limited at different depths z : (a) 500 m, (b) 1300 m, (c) 2100 m, (d) 2900 m, (e) 3700 m, and (f) 4500 m [98].

Figure 28 shows that the value of 3D density contrast distributions ranging from 500 m to 4500 m for a $220 \text{ km} \times 380 \text{ km}$ area was obtained by carrying out Occam's inversion with the rapid forward algorithm. The 3D density distribution given in this paper is compared with Figure 27, provided by Mira Geoscience Limited. Both are affected by the volume effect [83], superposition principle [75], and skin effect [28,99], resulting in excess smoothness in the horizontal direction. This leads to blurring between neighboring anomaly sources, making it difficult to differentiate them. In the depth direction, the depth resolution information of 3D density distributions is not efficiently obtained from either result.

Figure 29 shows the detailed density contrast distribution model of the QUEST-South project obtained using the RRCCG-based multilevel inversion. Compared with the 3D density contrast distributions of Occam's inversion in Figures 27 and 28, in the horizontal direction and on different depth slices, the 3D density contrast distribution obtained using the multilevel inversion has a better differentiation ability for neighboring anomaly sources. At different depths, whether positive or negative anomalies, the 3D density contrast distributions of the multilevel inversion have better depth resolution for neighboring anomaly sources.

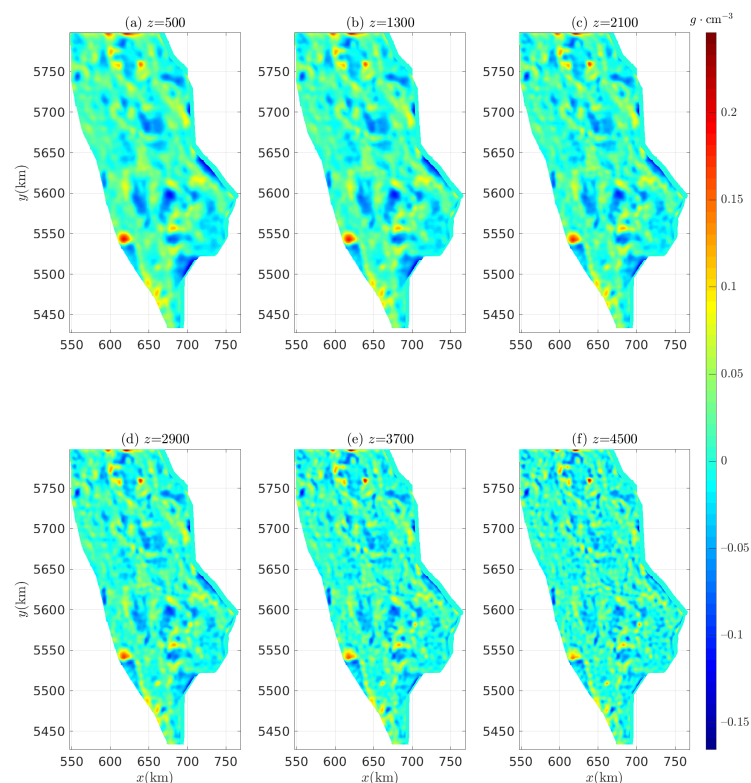


Figure 28. Inversion density distributions using Occam's inversion code at different depths z : (a) 500 m, (b) 1300 m, (c) 2100 m, (d) 2900 m, (e) 3700 m, and (f) 4500 m.

Compared with the results of the two synthetic models, the multilevel inversion has a good convergence tendency; however, due to the effect of the Haar wavelet, the data residuals still only match the high-frequency part of the original data (see Figure 26) from the appearance alone, so the low-energy, high-frequency noise does not affect the inversion results, but it may lead to unstable convergence of subsequent residual-corrected inversions, as shown in Figures 30 and 31.

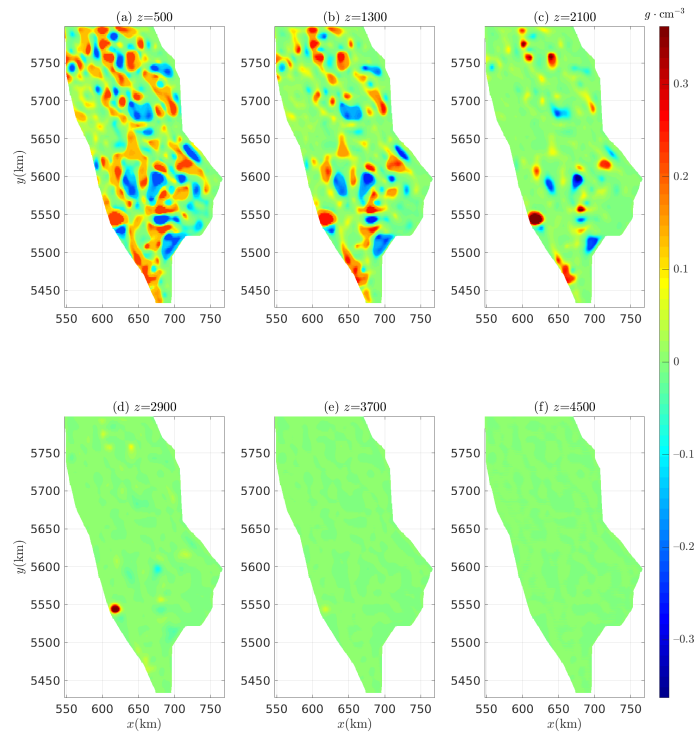


Figure 29. Inversion density distributions using the multilevel inversion at different depths z : (a) 500 m, (b) 1300 m, (c) 2100 m, (d) 2900 m, (e) 3700 m, and (f) 4500 m.

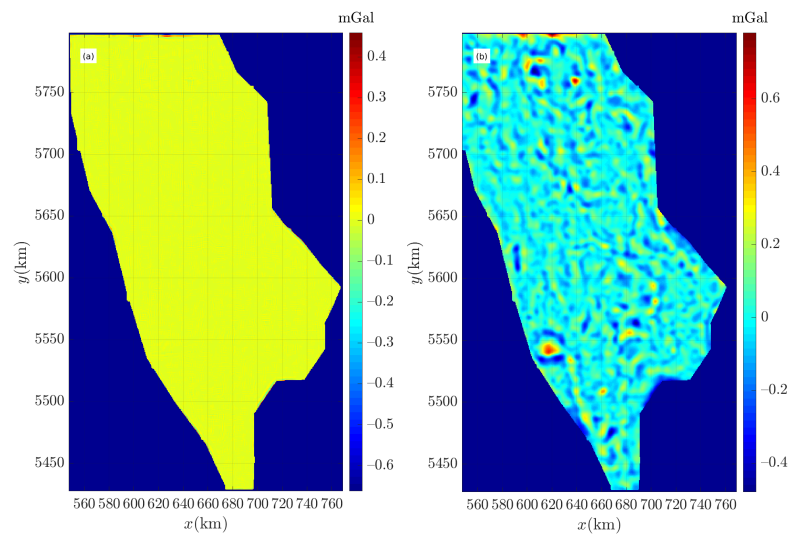


Figure 30. Residuals between observed and predicted data obtained by (a) Occam's inversion; and (b) multilevel inversion.

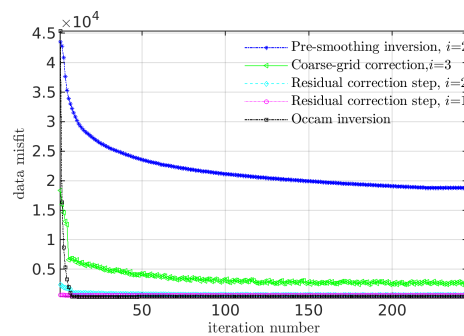


Figure 31. Data misfit obtained by Occam's and multilevel inversion.

The “ripple” phenomenon in the residual map (see Figure 23a) does not appear in Figure 30a. We speculate that a single anomalous source controls the former, while the latter has multiple anomalous sources. Furthermore, similar to Figure 23a, there are boundary band anomalies in Figure 30a. Similar to the results in Figure 23b, the multilevel inversion results are more focused due to the influence of the overfocusing effect of the RRCG solver, which leads to the formation of multiple “peaks” in the residual map. However, compared with the observation data, the data residuals are smaller, which shows the correctness of the algorithm proposed in this paper.

12. Model Plausibility Analysis

In order to enhance the credibility of the manuscript, we refer to related articles [37,55,100,101] and utilize histograms to assess the reasonableness of the recovered models. Due to the limited length of the paper, the histograms are employed only to analyze the data residuals and the recovered model of the field data.

Figures 32 and 33 show a different distribution from the histogram results in articles [37,55,100,101], which is due to the use of actual data and the interpretation models with sizes of 1024×1024 and $1024 \times 1024 \times 24$, with a large amount of sample data involved in the analysis. Taking Figure 32 as an example, Occam’s inversion is a smooth inversion, which means that the density values between adjacent physical units are smooth, and the corresponding predicted data and data residuals are also gradual (only when there are no jumps). Due to the smoothing effect, a large number of 0 values will appear (as shown in Figures 32 and 33, where the mean and standard deviation tend to be 0). Therefore, we plot the y-coordinate of the histogram in logarithmic form. At this point, Figure 32a presents a normal distribution in a logarithmic state, while Figure 32b shows several discontinuous values (in fact, the corresponding sample number is very small), which is consistent with the ambiguous values appearing at the upper-left boundary of Figure 30a. If these ambiguous values are excluded, Figure 32b can still be considered as a normal distribution. Compared to Figure 32a, the histogram result in Figure 33a only shows a peak in a range close to 0. Based on the analysis in Figure 29, we infer that this is related to the ability of the Haar wavelet to distinguish adjacent anomalies, that is, the Haar wavelet can effectively suppress small gradient values between adjacent anomalies, thereby improving the ability to distinguish adjacent anomaly sources. This also causes a large number of “ripples”, appearing in Figure 30b, leading to a larger corresponding standard deviation. From the histogram results of the reconstructed density model and the data residuals, compared to Occam’s inversion, it is reflected that there is no obvious ambiguity in the multi-layer inversion, and it has a good ability to discriminate adjacent anomaly sources.

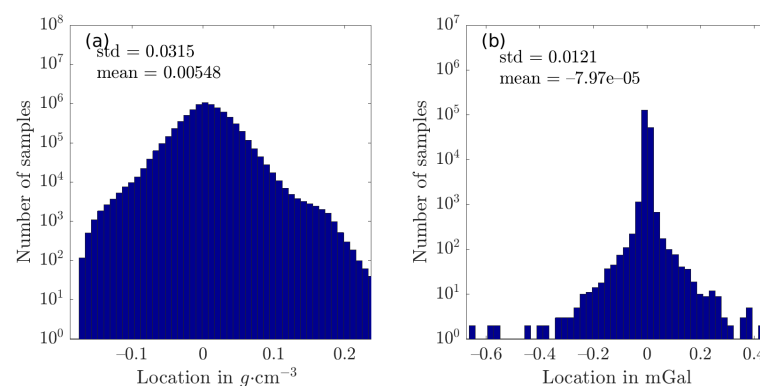


Figure 32. Histogram of the recovered model (a) and the data residual (b) with corresponding mean and standard deviation (std) for Occam’s inversion.

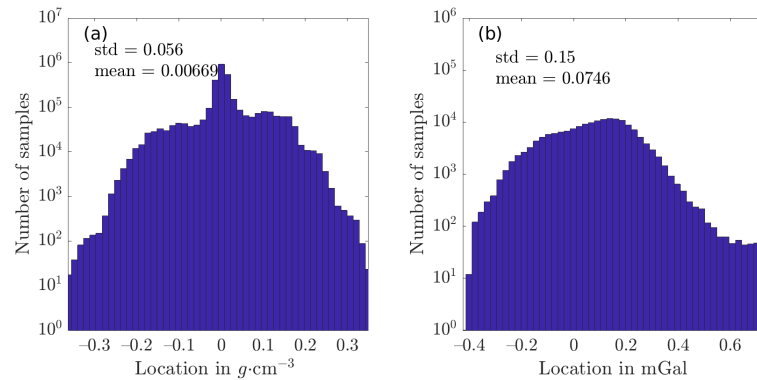


Figure 33. Histogram of the recovered model (a) and the data residual (b) with corresponding mean and standard deviation (std) for multilevel inversion.

13. Conclusions and Suggestions

Due to the use of forward and inverse operators based on the structure matrix, the inversion method proposed in this paper is not suitable for terrain data; compared with the traditional physical property inversion, the multilevel inversion has some difficulties in implementation. For example, due to the different characteristics of different gravity field components, there may be some differences in the transmission of the kernel matrix between the two adjacent layers, so it is also necessary to handle the corresponding programming work very carefully.

Compared with the physical property inversion method, the inversion method proposed in this paper does not need to store and calculate the inversion kernel matrix, which has extremely high execution efficiency and convergence speed. In comparison to the smooth inversion based on the L2 norm, the proposed inversion method has good depth and lateral resolution due to the use of the RRCCG solver and Haar wavelet. The acquisition of depth resolution information depends on the RRCCG solver, and there is still no good solution.

Due to the reliance on the symmetry of gravitational fields, the equivalent geometric framework is difficult to generalize to forward modeling of the tensor gravity components. Only translational equivalence is used to propose the extension equivalent geometric framework technology. Rapid forward algorithms can take advantage of small memory consumption to achieve significant acceleration capability, especially when using OpenMP technology with 56 threads. The efficiency of multilevel inversion is very high due to the use of a rapid forward algorithm and operator (Equation (42)). This operator is more concise than the solution to the computational problem in Español and Kilmer [68], and greatly solves the problem of kernel function transfer between different layers of an algebraic multigrid.

The classical multilevel methods are not immediately applicable to ill-posed problems [102–105], i.e., the deblurring problem, which often occurs in the geophysical science of forward/inverse. Therefore, to overcome this difficulty, we extended the multilevel methods from 2D to 3D, and the numerical results show that the multilevel methods are efficient solvers. Referring to Español's PhD thesis [106], the extension of multilevel methods from 2D to 3D is also the goal of their research. Moreover, this extension is not direct. Due to the influence of field source attenuation characteristics, the superposition effect, and the equivalence principle, the skin effect of physical property inversion became more and more severe. Even if the depth-weighting matrix was used, it was difficult to obtain the depth resolution information. In addition, affected by the smoothing effect, the traditional property inversion method based on the minimization of the sum-of-squares or L2 norm was smooth in both the vertical and horizontal directions [107].

This paper proposes an inversion framework that is more efficient for inter-layer transmission than the multigrid framework. In this paper, we solved the inversion problem of large-scale gravity/tensor gravity data based on RRCCG rather than the traditional

regularization method. This allowed us to reconstruct the density distribution with good depth resolution rather than being unable to distinguish adjacent anomalies and extract geological structure boundaries with good lateral resolution.

To avoid the impact of the actual observation data of the irregular boundary in Figure 22 on the inversion of the 3D density distribution results, this paper used the taper2d function to expand the data to grid data with $n_x = n_y = 2^{n_{max}}$. Once the inversion process was finished, the extended data and model were eliminated to ensure that the final inversion results accurately reflected the actual situation.

In this paper, there was no prior input of a priori geological information in the inversions of the two synthetic models and the actual data; the result of the previous stage of the multilevel inversion was used as a reference model for the subsequent stage of the inversion. If the previous results tend to be unstable, it will lead to the subsequent inversion results also tending to be unstable. However, the inversion results were obtained by the RRCG algorithm, and in the case where the RRCG algorithm was terminated by satisfying the convergence condition, stable results were obtained most of the time; in the case where the RRCG algorithm was terminated by not satisfying the convergence condition, at this point, we forced the RRCG algorithm not to output the results, which then led to the termination of the multilevel inversion. Due to the Haar wavelet, the high-frequency noise was inverted in the residual correction. When using the results of the previous pre-smoothing inversion as a reference model, these high-frequency noises with low energy did not affect the inversion results. However, they may have led to an unstable convergence of the inversion with the subsequent residual correction.

All the algorithms analyzed in this paper had several parameters that needed to be fine-tuned, e.g., the regularization parameter α , the decay index β , the number of V-cycles n , the coefficients of e , the minimum support functional W_e , and the number of iteration terminations of RRCG. In future studies, a better understanding of these parameters and the combination of the automatic selection function will be crucial for practical applications.

The Haar wavelet was introduced into our inversion, which can improve the lateral resolution of the reconstructed density distribution while preserving the structural properties of the kernel matrix. When considering the 2D case, it was very similar to the wavelet transform processing image. After the wavelet decomposition, the four submatrices of Equation (39) contained different frequency information from the original matrix. Among them, \overline{G}_{11} corresponded to low-frequency information, so its characteristics in potential field inversion were very similar to the original matrix \overline{G} . According to our limited knowledge, there are many kinds of wavelets that can retain the structural characteristics of the kernel matrix, such as the biorthogonal wavelet families: Biorthogonal Spline and Reverse Biorthogonal Spline; and orthogonal wavelet families: Daubechies, Beylkin, Coiflets, and Haar wavelets. For this reason, we suggest that interested readers can use the multilevel inversion framework proposed in this paper to deal with other special structural problems (e.g., Toeplitz structure, displacement structure) [108] with the help of the above wavelet operators. While preserving the structural properties of the kernel matrix at each level, other unique information is extracted, such as the faults, boundaries and directional lines of geological structures, and so on.

Author Contributions: Conceptualization, S.C.; methodology, S.C.; software, S.C., P.C. and D.Z.; validation, Y.M., D.Z. and Y.D.; formal analysis, S.C., P.C. and Y.M.; investigation, D.Z.; resources, G.L.; data curation, D.Z.; writing—original draft preparation, S.C., P.C. and G.L.; writing—review and editing, S.C., P.C., G.L. and X.C.; visualization, Y.M., P.C. and Y.D.; supervision, G.L. and X.C.; project administration, S.C., G.L. and X.C.; funding acquisition, G.L. All authors have read and agreed to the published version of the manuscript.

Funding: This research was funded by the National Natural Science Foundation of China under Grant 41704138 and Grant 41974148, in part by the Hunan Provincial Science & Technology Department of China under Grant 2017JJ3069, in part by the Project of the Doctoral Foundation of Hunan University

of Science and Technology under Grant E51651, and in part by the Hunan Provincial Key Laboratory of Share Gas Resource Exploitation under Grant E21722.

Data Availability Statement: Data are contained within the article.

Acknowledgments: We acknowledge the SEG/EAGE 3-D Modeling Committee for making the salt model available. We appreciate the Geoscience BC project for making the field data and the density distribution model available, which are freely accessible at <https://www.geosciencebc.com/major-projects/quest-south/> and <https://www.geosciencebc.com/projects/2009-025/> (accessed on 17 December 2023). The authors thank Zhengyong Ren of Central South University for their helpful suggestions.

Conflicts of Interest: The authors declare no conflicts of interest. The funders had no role in the design of the study; in the collection, analyses, or interpretation of data; in the writing of the manuscript, or in the decision to publish the results.

Abbreviations

The following abbreviations are used in this manuscript:

RRCG	Re-weighted regularized conjugate gradient
PDEs	Partial differential Equations
BTTB	Block-Toeplitz Toeplitz-Block
FFT	Fast Fourier transform
SEG	Society of Exploration Geophysicists
EAGE	European Association of Geoscientists & Engineers
FTG	Full tensor gravity

Symbol table

G_{ij}	The kernel function
α	The regularization parameter
$\phi_d(m)$	A data misfit (data misfit is defined by a least-squares measure) functional
$\phi_m(m)$	The model misfit function, also referred to as the model roughness
W_d	Data weighting matrix
T	The matrix transposition operation
β	The decay index
v	The gravitational constant
g	An irrotational field
$\bar{G}_{q,m}$	The sensitivity matrix for the Line–Line survey scheme
$G_{t,n}$	A BTTB matrix, also a kind of Toeplitz-like matrix
$\bar{\rho}_m$	The density vector for the m -th column prismatic cells
\bar{d}_q	The observation vector
W and W^T	Haar wavelet transform pairs
$E \otimes F$	The Kronecker product of E and F
$\bar{m}_{1,ref}$ and $\bar{m}_{2,ref}$	A wavelet domain reference model
W_e	The minimum support functional
e	A very small positive number

References

1. Cuma, M.; Wilson, G.A.; Zhdanov, M.S. Large-scale 3D inversion of potential field data. *Geophys. Prospect.* **2012**, *60*, 1186–1199. [[CrossRef](#)]
2. Chen, Z.X.; Meng, X.H.; Guo, L.H.; Liu, G.F. Three-dimensional fast forward modeling and the inversion strategy for large scale gravity and gravimetry data based on GPU. *Chin. J. Geophys.* **2012**, *55*, 4069–4077. (In Chinese)
3. Li, Y.; Oldenburg, D.W. Fast inversion of large-scale magnetic data using wavelet transforms and a logarithmic barrier method. *Geophys. J. Int.* **2003**, *152*, 251–265. [[CrossRef](#)]
4. Kellogg, O.D. *Foundations of Potential Theory*; Springer Nature: New York, NY, USA, 1929; Volume 31, pp. 354–355. [[CrossRef](#)]
5. Novák, P. Geoid determination using one-step integration. *J. Geod.* **2003**, *77*, 193–206. [[CrossRef](#)]
6. Marchenko, A.N. *Parameterization of the Earth's Gravity Field*; Lviv Astronomical and Geodetical Society: Lviv, Ukraine, 1998; pp. 34–40.
7. Tenzer, R.; Klees, R. The choice of the spherical radial basis functions in local gravity field modeling. *Stud. Geophys. Geod.* **2008**, *52*, 287–304. [[CrossRef](#)]

8. Tenzer, R.; Prutkin, I.; Klees, R. A comparison of different integral-equation-based approaches for local gravity field modelling: Case study for the Canadian Rocky Mountains. *IAG Symp.* **2012**, *136*, 381–388. [[CrossRef](#)] [[PubMed](#)]
9. Cavsak, H. Effective calculation of gravity effects of uniform triangle polyhedra. *Stud. Geophys. Geod.* **2012**, *56*, 185–195. [[CrossRef](#)]
10. Bhattacharyya, B.K.; Kuang, L. Spectral analysis of gravity and magnetic anomalies due to rectangular prismatic bodies. *Geophysics* **1977**, *42*, 41–50. [[CrossRef](#)]
11. Cao, S.J.; Zhu, Z.J.; Lu, G.Y.; Zeng, S.G.; Guo, W.B. Forward modelling of full gravity gradient tensors based on H-Adaptive mesh refinement. *Prog. Geophys.* **2010**, *25*, 1015–1023. (In Chinese) [[CrossRef](#)]
12. Zhdanov, M.S.; Ellis, R.; Mukherjee, S. Three-dimensional regularized focusing inversion of gravity gradient tensor component data. *Geophysics* **2004**, *69*, 925–937. [[CrossRef](#)]
13. Li, X.; Chouteau, M. Three-dimensional gravity modeling in all space. *Surv. Geophys.* **1998**, *19*, 339–368. [[CrossRef](#)]
14. Du, J.; Chen, C.; Liang, Q.; Wang, L.; Zhang, Y.; Wang, Q. Gravity anomaly calculation based on volume integral in spherical cap and comparison with the Tesseroid-Taylor series expansion approach. *Acta Geod. Cartogr. Sin.* **2012**, *41*, 339–346. (In Chinese)
15. Tsoulis, D. Analytical computation of the full gravity tensor of a homogeneous arbitrarily shaped polyhedral source using line integrals. *Geophysics* **2012**, *77*, F1–F11. [[CrossRef](#)]
16. Zhou, X. 3D vector gravity potential and line integrals for the gravity anomaly of a rectangular prism with 3D variable density contrast. *Geophysics* **2009**, *74*, IND-Z107. [[CrossRef](#)]
17. Camacho, A.G.; Fernández, J.; Gottsmann, J. The 3-D gravity inversion package GROWTH2.0 and its application to Tenerife Island, Spain. *Comput. Geosci.* **2011**, *37*, 621–633. [[CrossRef](#)]
18. Farquharson, C.G.; Mosher, C.R.W. Three-dimensional modelling of gravity data using finite differences. *J. Appl. Geophys.* **2009**, *68*, 417–422. [[CrossRef](#)]
19. Xu, S.Z. *The Finite Element Method in Geophysics*; Scientific Press: Beijing, China, 1994; pp. 215–219. (In Chinese)
20. Jahandari, H.; Farquharson, C.G. Forward modeling of gravity data using finite-volume and finite-element methods on unstructured grids. *Geophysics* **2013**, *78*, G69–G80. [[CrossRef](#)]
21. Cuma, M.; Zhdanov, M.S. Massively parallel regularized 3D inversion of potential fields on CPUs and GPUs. *Comput. Geosci.* **2014**, *62*, 80–87. [[CrossRef](#)]
22. Moorkamp, M.; Jegen, M.; Roberts, A.; Hobbs, R. Massively parallel forward modeling of scalar and tensor gravimetry data. *Comput. Geosci.* **2010**, *36*, 680–686. [[CrossRef](#)]
23. Chen, Z.; Meng, X. The GPU tests of 3-D constrained inversion for large-scale potential field data. In Proceedings of the 27th Annual Meeting of the Chinese Geophysical Society, Beijing, China, 18–21 October 2011; p. 694. (In Chinese)
24. Yao, C.; Hao, T.; Guan, Z.; Zhang, Y. High-speed computation and efficient storage in 3-D gravity and magnetic inversion. *Chin. J. Geophys.* **2003**, *46*, 351–361. [[CrossRef](#)]
25. Shin, Y.H.; Choi, K.S.; Xu, H. Three-dimensional forward and inverse models for gravity fields based on the fast Fourier transform. *Comput. Geosci.* **2006**, *32*, 727–738. [[CrossRef](#)]
26. Hou, Z.; Huang, D.; Wei, X. Fast inversion of probability tomography with gravity gradiometry data based on hybrid parallel programming. *J. Appl. Geophys.* **2016**, *124*, 27–38. [[CrossRef](#)]
27. Hou, Z.L.; Wei, X.H.; Huang, D.N.; Sun, X. Full tensor gravity gradiometry data inversion: Performance analysis of parallel computing algorithms. *Appl. Geophys.* **2015**, *12*, 292–302. [[CrossRef](#)]
28. Li, Y.; Oldenburg, D. 3-D inversion of gravity data. *Geophysics* **1998**, *63*, 109–119. [[CrossRef](#)]
29. Pilkington, M. 3-D magnetic imaging using conjugate gradients. *Geophysics* **1997**, *62*, 1132–1142. [[CrossRef](#)]
30. Meng, Z. 3D inversion of full gravity gradient tensor data using SL0 sparse recovery. *J. Appl. Geophys.* **2016**, *127*, 112–128. [[CrossRef](#)]
31. Cao, S.; Zhu, Z.; Lu, G. Gravity inversion based on hyper-parameter regularization inversion via iteration splitting Bregman algorithm. *J. Cent. South Univ.* **2015**, *46*, 1699–1706. (In Chinese)
32. Constable, S.C.; Parker, R.L.; Constable, C.G. Occam's inversion: A practical algorithm for generating smooth models from electromagnetic sounding data. *Geophysics* **1987**, *52*, 289–300. [[CrossRef](#)]
33. Meng, Z. Research on 3D gravity inversion based on LP norm minimization. In *Topic 3: Collection of Papers on Earth Gravity Field and Its Geological Applications, Proceedings of the 2014 China Earth Science Joint Academic Annual Conference, Beijing, China, 20–23 October 2014*; Annual Meeting of Chinese Geoscience Union: Beijing, China, 2014; p. 1. (In Chinese)
34. Farquharson, C.G.; Ash, M.R.; Miller, H.G. Geologically constrained gravity inversion for the Voisey's Bay ovoid deposit. *Lead. Edge* **2008**, *27*, 64–69. [[CrossRef](#)]
35. Lima, W.A.; Martins, C.M.; Silva, J.B.C.; Barbosa, V.C.F. Total variation regularization for depth-to-basement estimate: Part 2—Physicogeologic meaning and comparisons with previous inversion methods. *Geophysics* **2011**, *76*, I13–I20. [[CrossRef](#)]
36. Martins, C.M.; Lima, W.A.; Barbosa, V.C.F.; Silva, J.B.C. Total variation regularization for depth-to-basement estimate: Part 1—Mathematical details and applications. *Geophysics* **2011**, *76*, I1–I12. [[CrossRef](#)]
37. Portniaguine, O.; Zhdanov, M. Focusing geophysical inversion images. *Geophysics* **1999**, *64*, 874–887. [[CrossRef](#)]
38. Zhang, L.; Yu, P.; Wang, J.; Wu, J. Smoothest model and sharp boundary based two-dimensional magnetotelluric inversion. *Chin. J. Geophys.* **2009**, *52*, 1625–1632. [[CrossRef](#)]

39. Yi-xin, Y.; Yu-ping, C. Application analysis of sharp boundary inversion of magnetotelluric data for 2D structure. *Prog. Geophys.* **2009**, *24*, 668–674. (In Chinese)
40. Huang, S. Regularization algorithm research of static electrical impedance tomography. PhD Thesis, Chongqing University, Chongqing, China, 2005. (In Chinese)
41. Yue, J.H. Research of mixture regularization methods for EIT inverse problem. Master's Thesis, Dalian Maritime University, Dalian, China, 2012. (In Chinese)
42. Zhdanov, M.S.; Vignoli, G.; Ueda, T. Sharp boundary inversion in crosswell travel-time tomography. *J. Geophys. Eng.* **2006**, *3*, 122–134. [[CrossRef](#)]
43. Mehanee, S.; Zhdanov, M. Two-dimensional magnetotelluric inversion of blocky geoelectrical structures. *J. Geophys. Res. Solid Earth* **2002**, *107*, 279–282. [[CrossRef](#)]
44. Abubakar, A.; Habashy, T.M.; Li, M.; Liu, J. Inversion algorithms for large-scale geophysical electromagnetic measurements. *Inverse Probl.* **2009**, *25*, 1541–1548. [[CrossRef](#)]
45. Cardarelli, E.; Fischanger, F. 2D data modelling by electrical resistivity tomography for complex subsurface geology. *Geophys. Prospect.* **2006**, *54*, 121–133. [[CrossRef](#)]
46. Commer, M.; Newman, G.A. New advances in three-dimensional controlled-source electromagnetic inversion. *Geophys. J. Int.* **2008**, *172*, 513–535. [[CrossRef](#)]
47. Wilson, G.A.; Cox, L.H.; Cuma, M.; Zhdanov, M.S. Inverting airborne geophysical data for mega-cell and giga-cell 3D Earth models. *Lead. Edge* **2012**, *31*, 316–321. [[CrossRef](#)]
48. Wilson, G.A.; Cuma, M.; Zhdanov, M.S. Massively parallel 3D inversion of gravity and gravity gradiometry data. *Preview* **2011**, *2011*, 29–34. [[CrossRef](#)]
49. Zhdanov, M.S.; Endo, M.; Cox, L.H.; Cuma, M.; Linfoot, J.; Anderson, C.; Black, N.; Gribenko, A.V. Three-dimensional inversion of towed streamer electromagnetic data. *Geophys. Prospect.* **2014**, *62*, 552–572. [[CrossRef](#)]
50. Vatankhah, S.; Renaut, R.A.; Huang, X.; Mickus, K.; Gharloghi, M. Large-scale focusing joint inversion of gravity and magnetic data with Gramian constraint. *Geophys. J. Int.* **2022**, *230*, 1585–1611. [[CrossRef](#)]
51. Boulanger, O.; Chouteau, M. Constraints in 3D gravity inversion. *Geophys. Prospect.* **2001**, *49*, 265–280. [[CrossRef](#)]
52. Last, B.J.; Kubik, K. Compact gravity inversion. *Geophysics* **1983**, *48*, 713–721. [[CrossRef](#)]
53. Commer, M. Three-dimensional gravity modelling and focusing inversion using rectangular meshes. *Geophys. Prospect.* **2011**, *59*, 966–979. [[CrossRef](#)]
54. Zhdanov, M.S.; Smith, R.B.; Gribenko, A.; Cuma, M.; Green, M. Three-dimensional inversion of large-scale EarthScope magnetotelluric data based on the integral equation method: Geoelectrical imaging of the Yellowstone conductive mantle plume. *Geophys. Res. Lett.* **2011**, *38*, L08-307. [[CrossRef](#)]
55. Rezaie, M.R.; Moradzadeh, A.; Kalate, A.N.; Aghajani, H. Fast 3D focusing inversion of gravity data using reweighted regularized lanczos bidiagonalization method. *Pure Appl. Geophys.* **2016**, *174*, 359–374. [[CrossRef](#)]
56. Debnath, L. *Wavelet Transforms and Their Applications*; Springer: Berlin/Heidelberg, Germany, 2002; p. 68. [[CrossRef](#)]
57. Bao, G. New advance of multiscale geometric analysis: Contourlet. *Comput. Sci.* **2006**, *33*, 234–236.
58. Zhao, Q.M. Application study on Curvelet transform in face recognition. *Comput. Sci.* **2013**, *13*, 38–40.
59. Frangakis, A.S.; Stoschek, A.; Hegerl, R. Wavelet transform filtering and nonlinear anisotropic diffusion assessed for signal reconstruction performance on multidimensional biomedical data. *IEEE Trans. Biomed. Eng.* **2001**, *48*, 213–222. [[CrossRef](#)] [[PubMed](#)]
60. Li, Y.; Hu, J. Research on SAR image denoising method based on curvelet and wavelet. *Adv. Eng. Sci.* **2011**, *44*, 145–149. (In Chinese)
61. Hao, Z.; Feng, F.; Wang, D.; Zhao, W. Research on OBC multiple wave attenuation method in Curvelet domain. *Global Geol.* **2013**, *32*, 130–136.
62. Liu, M.; Wu, J.; Yu, P.; Zhang, L. 2D wavelet decomposition based two-dimensional magnetotelluric inversion. *Geophys. Geochem. Explor.* **2009**, *33*, 337–341.
63. Ren, H.; Yang, W.; Wang, J. A method of image denoising based on multiresolution morphological pyramid. *Comput. Eng.* **2004**, *30*, 136–137.
64. Zheng, G. Research and development of fast pyramid generation algorithm for massive remote sensing image. Ph.D. Thesis, East China Normal University, Shanghai, China, 2012. (In Chinese)
65. Bousquet, A.; Marion, M.; Petcu, M.; Temam, R. Multilevel finite volume methods and boundary conditions for geophysical flows. *Comput. Fluids* **2013**, *74*, 66–90. [[CrossRef](#)]
66. Bolten, M.; Donatelli, M.; Huckle, T.; Kravvaritis, C. Generalized grid transfer operators for multigrid methods applied on Toeplitz matrices. *BIT Numer. Math.* **2015**, *55*, 341–366. [[CrossRef](#)]
67. Buccini, A.; Donatelli, M. A multigrid frame based method for image deblurring. *Electron. Trans. Numer. Anal.* **2020**, *53*, 283–312. [[CrossRef](#)]
68. Español, M.I.; Kilmer, M.E. Multilevel Approach For Signal Restoration Problems With Toeplitz Matrices. *SIAM J. Sci. Comput.* **2010**, *32*, 299–319. [[CrossRef](#)]
69. Chung, J.; Kilmer, M.E.; O'Leary, D.P. A Framework for Regularization via Operator Approximation. *SIAM J. Sci. Comput.* **2015**, *37*, B332–B359. [[CrossRef](#)]

70. Chu, Z.; Yan, Z.; Li, C. A New Extrapolation Economy Cascadic Multigrid Method for Image Restoration Problems. *Am. J. Comput. Math.* **2023**, *13*, 323–341. [[CrossRef](#)]
71. Yang, H.; Zhang, R. A fast multilevel iteration method for solving linear ill-posed integral equations. *J. Inverse Ill-Posed Probl.* **2021**, *30*, 409–423. [[CrossRef](#)]
72. Williams, N.C. Geologically-constrained UBC-GIF gravity and magnetic inversions with examples from the Agnew-Wiluna greenstone belt, Western Australia. Ph.D. Thesis, The University of British Columbia, Vancouver, BC, USA, 2008. [[CrossRef](#)]
73. Zhdanov, M.S. *Integral Transforms in Geophysics*; Springer: Berlin/Heidelberg, Germany, 1988; pp. 140–143. [[CrossRef](#)]
74. Vestine, E.H.; Davids, N. Analysis and interpretation of geomagnetic anomalies. *Terr. Magn. Atmos. Electr.* **1945**, *50*, 1–36. [[CrossRef](#)]
75. Blakely, R.J. *Potential Theory in Gravity and Magnetic Applications*; Cambridge University Press: Cambridge, UK, 1996; pp. 31–32. [[CrossRef](#)]
76. Zhang, G.; Zhang, G.; Jin, F.; Meng, L. Research on regularized equal-dimensional inversion of gravity anomaly. In Proceedings of the Gravity and Magnetic Data Processing Interpretation Application Seminar, Hangzhou, China, 15–18 April 2008; China University of Geosciences: Wuhan, China, 2008. (In Chinese)
77. Chan, R.H.; Jin, X.Q. *An Introduction to Iterative Toeplitz Solvers*; SIAM: Philadelphia, PA, USA, 2007; p. 1. [[CrossRef](#)]
78. Sima, D.M.; Huffel, S.V.; Golub, G.H. Regularized total least squares based on quadratic eigenvalue problem solvers. *BIT Numer. Math.* **2004**, *44*, 793–812. [[CrossRef](#)]
79. Björck, A. *Numerical Methods for Least Squares Problems*; SIAM: Philadelphia, PA, USA, 1996; pp. 336–338.
80. Tu, X.; Zhdanov, M.S. Enhancement and sharpening the migration images of the gravity field and its gradients. *Pure Appl. Geophys.* **2019**, *177*, 2853–2870. [[CrossRef](#)]
81. Zhdanov, M.S. *Geophysical Inverse Theory and Regularization Problem*; Elsevier: Amsterdam, The Netherlands, 2002; pp. 155–165.
82. Zhdanov, M.S. Inverse Theory and Applications in Geophysics. In *Inverse Theory and Applications in Geophysics*; Springer: New York, NY, USA, 2015; pp. 1–704. [[CrossRef](#)]
83. May, D.A.; Knepley, M.G. Optimal, scalable forward models for computing gravity anomalies. *Geophys. J. Int.* **2011**, *187*. [[CrossRef](#)]
84. Zhdanov, M.S.; Endo, M.; Yoon, D.; Cuma, M.; Mattsson, J.; Midgley, J. Anisotropic 3D inversion of towed-streamer electromagnetic data: Case study from the Troll West Oil Province. *Interpretation* **2014**, *2*, 552–572. [[CrossRef](#)]
85. Aminzadeh, F.; Burkhard, N.; Nicoletis, L.; Rocca, F.; Wyatt, K. SEG/EAEG 3-D modeling project: 2nd update. *Lead. Edge.* **1994**, *13*, 949–952. [[CrossRef](#)]
86. Aminzadeh, F.; Weimer, P.; Davis, T. 3-D salt and overthrust seismic models. In *Applications of 3-D Seismic Data to Exploration and Production*; American Association of Petroleum Geologists: Tulsa, OK, USA, 1996; Volume 42, pp. 247–256. [[CrossRef](#)]
87. Cooper, G.; Cowan, D. Differential reduction to the pole. *Comput. Geosci.* **2005**, *31*, 989–999. [[CrossRef](#)]
88. Jensen, E.P.; Barton, M.D. Gold deposits related to alkaline magmatism. In *Gold in 2000*; Society of Economic Geologists: Littleton, CO, USA, 2000; Volume 13, pp. 10–13. [[CrossRef](#)]
89. Hanley, J.; Kerr, M.; LeFort, D.; Warren, M.; MacKenzie, M.; Sedge, C. Enrichment of platinum-group elements (PGE) in alkalic porphyry Cu-Au deposits in the Canadian Cordillera: New insights from mineralogical and fluid inclusion studies. *Porphyry Depos. Northwestern Cordill. North Am. A* **2020**, *25*, 88–109.
90. Thompson, J.F.; Lang, J.R.; Stanley, C.R. Platinum group elements in alkaline porphyry deposits, British Columbia. *Explor. Min. Br. Columbia, Mines Branch Part B* **2001**, *574*, 8–10.
91. Mitchinson, D. *Integrated Interpretation of Electromagnetic and Gravity Data to Resolve Deep Geology and Aid Mineral Exploration in the Quesnel Terrane, Central British Columbia (Parts of NTS 093A, B, G, H, J, K, N, O, 094C, D)*; Geoscience BC: Vancouver, BC, Canada, 2023; pp. 1–12.
92. Nelson, J.; Colpron, M.; Goodfellow, W. Tectonics and metallogeny of the British Columbia, Yukon and Alaskan Cordillera, 1.8 Ga to the present. In *Tectonics, Metallogeny, and Discovery: The North American Cordillera and Similar Accretionary Settings*; Society of Economic Geologists: Littleton, CO, USA, 2007; Volume 5, pp. 755–791. [[CrossRef](#)]
93. Sanchez, M.; Bissig, T.; Kowalczyk, P. *Interpretation Map of Magnetic and Gravity Datasets, QUEST Area, Central British Columbia*; Fault Rocks Consulting: Vancouver, BC, Canada, 2015; pp. 1–17.
94. Phillips, N.; Nguyen, T.; Thomson, V.; Oldenburg, D.; Kowalczyk, P. 3D inversion modelling, integration, and visualization of airborne gravity, magnetic, and electromagnetic data: The Quest project. In Proceedings of the EGM 2010 International Workshop, Capri, Italy, 11–14 April 2010. [[CrossRef](#)]
95. Reichheld, S. *Documentation and Assessment of Exploration Activities Generated by Geoscience BC Data Publications, QUEST Project, Central British Columbia (NTS 093A, B, G, H, J, K, N, O, 094C, D)*; Geoscience BC: Vancouver, BC, Canada, 2013; pp. 125–130.
96. Erdmer, P.; Cui, Y. Geological Map of British Columbia. British Columbia Ministry of Energy, Mines and Petroleum Resources, British Columbia Geological Survey Geoscience Map 2009-01, 1:1,500,000, 2009. Available online: <https://www2.gov.bc.ca/gov/content/industry/mineral-exploration-mining/british-columbia-geological-survey/publications/geosciencemaps#2009> (accessed on 14 March 2024).
97. France, B.; Martin, B. *Airborne Gravity Survey QUEST-South, British Columbia-2009 Geoscience British Columbia Society*; Technical Report, GeoScience BC QUEST South-2009; Sander Geophysics Limited: Ottawa, ON, Canada, 2009. Available online: https://cdn.geosciencebc.com/project_data/GBC_Report2010-6/GBC_Report2010-6_Technical_Report.pdf (accessed on 24 January 2024).

98. *Regional 3D Inversion Modelling of Airborne Gravity and Magnetic data: QUEST-South, BC, Canada*; Technical Report 14; Mira Geoscience: Vancouver, BC, Canada, 2011. Available online: https://cdn.geosciencebc.com/pdf/Presentations/Roundup11_Phillips.pdf (accessed on 7 January 2024).
99. Siripunvaraporn, W.; Sarakorn, W. An efficient data space conjugate gradient Occam's method for three-dimensional magnetotelluric inversion. *Geophys. J. Int.* **2011**, *186*, 567–579. [[CrossRef](#)]
100. Nagarajan, S.S.; Portniaguine, O.; Hwang, D.; Johnson, C.R.; Sekihara, K. Controlled Support MEG imaging. *NeuroImage* **2006**, *33*, 878–885. [[CrossRef](#)] [[PubMed](#)]
101. Vatankhah, S.; Huang, X.; Renaut, R.A.; Mickus, K.L.; Lin, J. Joint Gramian inversion of gravity, magnetic, and gravity gradient tensor data for the modeling of Mesoproterozoic iron oxide deposits, southeast Missouri, USA. *Geophys. J. Int.* **2023**, *235*, 1064–1085. [[CrossRef](#)]
102. Bollhöfer, M.; Grote, M.J.; Schenk, O. Algebraic Multilevel Preconditioner for the Helmholtz Equation in Heterogeneous Media. *SIAM J. Sci. Comput.* **2009**, *31*, 3781–3805. [[CrossRef](#)]
103. Fulton, S.R.; Ciesielski, P.E.; Schubert, W.H. Multigrid methods for elliptic problems: A review. *Mon. Weather Rev.* **1986**, *114*, 943–959. [[CrossRef](#)]
104. Koldan, J.; Puzyrev, V.; de la Puente, J.; Houzeaux, G.; Cela, J.M. Algebraic multigrid preconditioning within parallel finite-element solvers for 3-D electromagnetic modelling problems in geophysics. *Geophys. J. Int.* **2014**, *197*, 1442–1458. [[CrossRef](#)]
105. Pan, K.; Tang, J. 2.5-D and 3-D DC resistivity modelling using an extrapolation cascadic multigrid method. *Geophys. J. Int.* **2014**, *197*, 1459–1470. [[CrossRef](#)]
106. Malena, I.E. Multilevel methods for discrete ill-posed problems: Application to deblurring. Ph.D. Thesis, Tufts University, Medford, MA, USA, 2009.
107. Farquharson, C.G. Constructing piecewise-constant models in multidimensional minimum-structure inversions. *Geophysics* **2008**, *73*, K1–K9. [[CrossRef](#)]
108. Pruessner, A.; O'Leary, D.P. Blind Deconvolution Using a Regularized Structured Total Least Norm Algorithm. *SIAM J. Matrix Anal. Appl.* **2002**, *24*, 1018–1037. [[CrossRef](#)]

Disclaimer/Publisher's Note: The statements, opinions and data contained in all publications are solely those of the individual author(s) and contributor(s) and not of MDPI and/or the editor(s). MDPI and/or the editor(s) disclaim responsibility for any injury to people or property resulting from any ideas, methods, instructions or products referred to in the content.